GNOTHI SEAUTON: EMPOWERING FAITHFUL SELF-INTERPRETABILITY IN BLACK-BOX MODELS

Anonymous authors
Paper under double-blind review

ABSTRACT

The debate between self-interpretable models and post-hoc explanations for black-box models is central to Explainable AI (XAI). Self-interpretable models, such as concept-based networks, offer insights by connecting decisions to human-understandable concepts but often struggle with performance and scalability. Conversely, post-hoc methods like Shapley values, while theoretically robust, are computationally expensive and resource-intensive. To bridge the gap between these two lines of research, we propose a novel method that combines their strengths, providing theoretically guaranteed self-interpretability for black-box models without compromising prediction accuracy. Specifically, we introduce a parameter-efficient pipeline, *AutoGnothi*, which integrates a small side network into the black-box model, allowing it to generate Shapley value explanations without changing the original network parameters. This side-tuning approach significantly reduces memory, training, and inference costs, outperforming traditional parameter-efficient methods, where full fine-tuning serves as the optimal baseline. *AutoGnothi* enables the black-box model to predict and explain its predictions with minimal overhead. Extensive experiments show that *AutoGnothi* offers accurate explanations for both vision and language tasks, delivering superior computational efficiency with comparable interpretability.

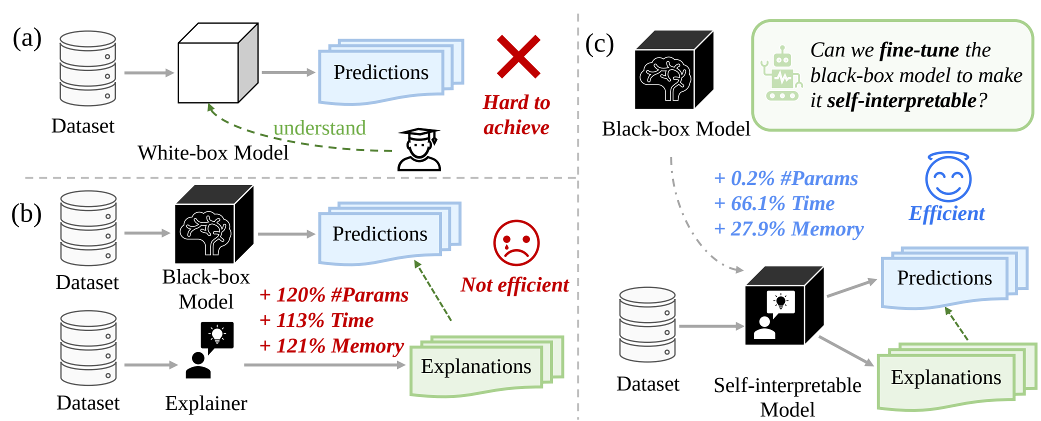

Figure 1: **Different paradigms towards XAI.** (a) The ideal paradigm for XAI envisions using white-box models for prediction, which are inherently self-interpretable by design but hard to achieve. (b) The previous paradigm involves post-hoc explanations of black-box models by training a separate, heavy-weight explainer. (c) We propose a novel parameter-efficient paradigm, *AutoGnothi*, which fine-tunes the black-box model to make it self-interpretable.

1 INTRODUCTION

Explainable AI (XAI) has gained increasing significance as AI systems are widely deployed in both vision (Dosovitskiy, 2020; Radford et al., 2021; Kirillov et al., 2023) and language domains (Devlin et al., 2019; Brown, 2020; Achiam et al., 2023). Ensuring interpretability in these systems is vital for fostering trust, ensuring fairness, and adhering to legal standards, particularly for complex models such as transformers. As illustrated in Figure 1(a), the ideal paradigm for XAI involves designing inherently transparent models that deliver superior performance. However, given the challenges in achieving this, current XAI methodologies can be broadly classified into two main categories: developing *self-interpretable models* and providing *post-hoc explanations* for black-box models.

Designing Self-Interpretable Models: Several notable efforts have focused on designing self-interpretable models that are grounded in solid mathematical foundations or learned concepts. Among these, concept-based networks have emerged as a representative approach linking model decisions to predefined, human-understandable concepts (Kim et al., 2018; Koh et al., 2020; Alvarez-Melis & Jaakkola, 2018). However, incorporating hand-crafted concepts often introduces a trade-off between interpretability and performance, as these models typically compromise the performance of the primary task. Moreover, such methods are often closely tied to specific architectures, which limits their scalability and transferability to other tasks. Furthermore, the explanations generated by concept-based models often lack a rigorous theoretical foundation, raising concerns about their reliability and overall trustworthiness.

Explaining Black-Box Models: Given the challenges of designing self-interpretable models for practical applications, post-hoc explanations for black-box models have become a widely adopted alternative. Among these, Shapley value-based methods (Shapley, 1953) are particularly valued for their theoretical rigor and adherence to four principled axioms (Young, 1985). However, calculating exact Shapley values involves evaluating all possible feature combinations, which scales exponentially with the number of features, making direct computation impractical for models with high-dimensional inputs. To alleviate this, methods like FastSHAP (Jethani et al., 2021) and ViT-Shapley (Covert et al., 2022) employ proxy explainers that estimate Shapley values during inference, significantly reducing the number of evaluations needed. While these approaches reduce some computational costs, training a separate explainer remains resource-intensive. For example, training a Vision Transformer (ViT) explainer requires more than twice the training GPU memory compared to the ViT classifier itself. Moreover, solely depending on post-hoc explanations for black-box models is not ideal in high-stakes decision-making scenarios, where immediate and reliable interpretability is required (Rudin, 2019).

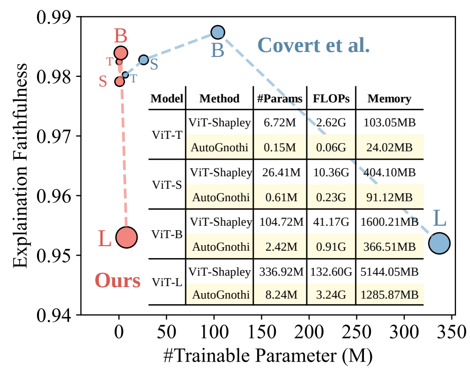

Model	Method	#Params	FLOPs	Memory
ViT-T	ViT-Shapley	6.72M	2.62G	103.05MB
	AutoGnothi	0.15M	0.06G	24.02MB
ViT-S	ViT-Shapley	26.41M	10.36G	404.10MB
	AutoGnothi	0.61M	0.23G	91.12MB
ViT-B	ViT-Shapley	104.72M	41.17G	1600.21MB
	AutoGnothi	2.42M	0.91G	366.51MB
ViT-L	ViT-Shapley	336.92M	132.60G	5144.05MB
	AutoGnothi	8.24M	3.24G	1285.87MB

Figure 2: **Explanation quality on the ImageNette dataset using different ViTs.** Our *AutoGnothi* significantly reduces the number of trainable parameters, computational costs (FLOPs), and training GPU memory storage without compromising explanation quality.

To bridge the gap between existing methods and address the aforementioned challenges, the core objective of our research is to *achieve theoretically guaranteed self-interpretability in advanced neural networks without sacrificing prediction performance, while minimizing training, memory, and inference costs*. To this end, we propose a novel paradigm, *AutoGnothi*, which leverages parameter-efficient transfer learning (PETL) to substantially reduce the high training, memory, and inference costs associated with obtaining explainers. As depicted in Figure 3(a), traditional model-specific methods require two training stages: (i) fine-tuning a pre-trained model into a surrogate model, and (ii) training an explainer using the surrogate model. During inference, the original model is used for prediction, while a separate explainer network generates explanations, leading to two inference passes and double the storage overhead. In contrast, *AutoGnothi* utilizes side-tuning to reduce both training and memory costs, as shown in Figure 3(b). By incorporating an additive side branch parallel to the pre-trained model, we efficiently obtain a surrogate side network through side-tuning. We then apply the same strategy to develop the explainer side network, enabling simultaneous prediction and explanation in a single inference step. An illustrative example comparing the efficiency of *AutoGnothi* with previous methods is presented in Figure 2.

More importantly, *AutoGnothi* achieves self-interpretability without compromising prediction accuracy. Unlike a simple application of PETL, where full fine-tuning is considered the optimal baseline, our approach goes further. Experimental results show that relying on full fine-tuning to achieve self-interpretability often leads to degraded performance in either prediction or explanation tasks. In contrast, *AutoGnothi* maintains prediction accuracy while achieving self-interpretability by lever-

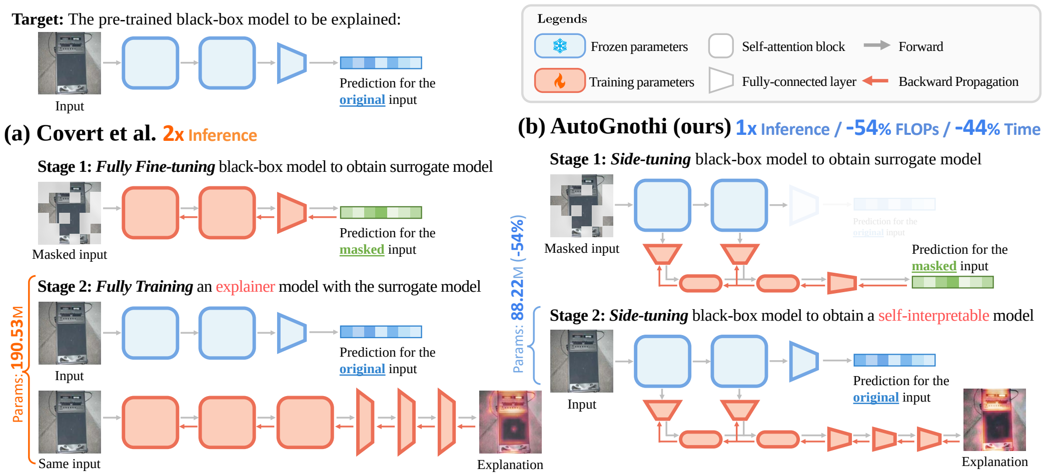

Figure 3: **Overview of *AutoGnothi* compared to prior work.** (a) ViT-Shapley (Covert et al., 2022) fully fine-tunes the black-box model to create a surrogate model, then trains a separate explainer based on the surrogate, which is resource-intensive. (b) We employ side-tuning to efficiently obtain both the black-box model and explainer, significantly reducing training costs. *AutoGnothi* uses a single model to simultaneously generate predictions and explanations, lowering inference costs by leveraging shared features. In contrast, ViT-Shapley needs to load two models for prediction and explanation, respectively, and infers two times. *AutoGnothi* enables self-interpretability for an arbitrary black-box model. We ignore the positional encoding associated with the pipeline.

aging the intrinsic correlation between prediction and explanation. Beyond classical PETL, which primarily focuses on training efficiency, *AutoGnothi* also enhances inference efficiency through self-interpretation while keeping its faithfulness (see Section 4.2 for further discussion). Our key contributions are as follows:

1. **Efficient Explanation**: We introduce a novel PETL pipeline, *AutoGnothi*, which enables any black-box models, *e.g.*, transformers, to become self-interpretable without affecting the original task parameters. By integrating and fine-tuning an additive side network, suprisingly surpasses previous methods in training, inference, and memory efficiency.
2. **Self-interpretability**: We achieve theoretically guaranteed self-interpretability for the black-box model with the Shapley value, without any influence on the original model's prediction accuracy.
3. **Broad Applications on both Vision and Language Models**: We conducted experiments on the most widely used models, including ViT (Dosovitskiy, 2020) for image classification and BERT (Devlin et al., 2019) for sentimental analysis, showing that our methods outperform well on explanation quality. Specifically, for the ViT-base model pre-trained on ImageNette, our surrogates achieve a 97% reduction in trainable parameters and 72% reduction in training memory with comparable accuracy. For explainers, we achieve a 98% reduction in trainable parameters, 77% reduction in training memory. For generating explanation, *AutoGnothi* achieves 54% reduction in inference computation, 44% reduction in inference time, and a total parameter reduction of 54%.

2 Related Work

Explaining Black-Box Models with Shapley Values: Among post-hoc explanation methods, the Shapley value (Shapley, 1953) is widely recognized as a faithful and theoretically sound metric for feature attribution, uniquely satisfying four key axioms: *efficiency*, *symmetry*, *linearity*, and *dummy*. However, computing Shapley values is computationally expensive, requiring $\mathcal{O}(2^n)$ operations to calculate a single Shapley value for one feature in a set of size n. To alleviate this computational burden, various approaches have been proposed to expedite Shapley value computation, which can be broadly divided into *model-agnostic* and *model-specific* methods (Chen et al., 2023a). Model-agnostic techniques, such as KernelSHAP (Lundberg, 2017) and its enhancements (Covert & Lee, 2020), approximate Shapley values by sampling subsets of feature combinations. Nevertheless, when the feature set is large, the sampling cost remains prohibitive, and reducing this cost compromises the accuracy of the explanations, as fewer samples lead to less reliable estimates of feature importance. Conversely, model-specific methods, such as FastSHAP (Jethani et al., 2021) and ViT-Shapley (Covert et al., 2022), employ a trained proxy explainer to accelerate the estimation during inference, though these methods still involve significant training costs to develop the explainer.

Parameter Efficient Transfer Learning (PETL): PETL aims to achieve the performance of full fine-tuning while significantly reducing training costs by updating only a small subset of parameters. In this context, Adapters (Houlsby et al., 2019; Chen et al., 2023b) introduce trainable bottleneck modules into transformer layers, enabling models to deliver competitive results with minimal parameter adjustments. Another widely adopted method, LoRA (Hu et al., 2021), applies low-rank decomposition to the attention layer weights. Our work aligns more closely with side-tuning methods, where Side-Tuning (Zhang et al., 2020) integrates an auxiliary network that merges its representations with the backbone at the final layer, demonstrating effectiveness across diverse tasks in models like ResNet and BERT. LST (Sung et al., 2022) further improves this approach by reducing memory consumption through a ladder side network design. However, none of these methods explore the transfer of interpretability from the main model to the side network, leaving this a largely unexplored area in side-tuning and PETL research.

3 Background

3.1 Shapley Values

The Shapley value, originally introduced in game theory (Shapley, 1953), provides a method to fairly distribute rewards among players in coalitional games. In this framework, a set function assigns a value to any subset of players, corresponding to the reward earned by that subset. In machine learning scenarios, input variables are typically regarded as players, and a deep neural network (DNN) serves as the value function, assigning importance (saliency) to each input variable.

Let $s \in \{0,1\}^d$ be an indicator vector representing a specific variable subset for a sample $x = [x_1, x_2, \dots, x_d]^\top \in \mathbb{R}^d$. Specifically, x_s denotes the variables indicated by s, while those not in s are replaced by a masked value (*e.g.*, a baseline value). Let $e_i \in \mathbb{R}^d$ denote the vector with a one in the i-th position and zeros elsewhere. For a game involving d players—or equivalently, a DNN $v : \{0,1\}^d \to \mathbb{R}$ with d input variables—the Shapley values are denoted by $\phi_v(x_1), \dots, \phi_v(x_d)$. Each $\phi_v(x_i) \in \mathbb{R}$ represents the value attributed to the i-th input variable x_i in the sample x. The Shapley value $\phi_v(x_i)$ is computed as follows:

$$\phi_v(x_i) = \frac{1}{d} \sum_{s: s_i = 0} \binom{d-1}{\mathbf{1}^\top s} \left(v(x_{s+e_i}) - v(x_s) \right). \tag{1}$$

Intuitively, Eq. (1) captures the average marginal contribution of the i-th player to the overall reward by considering all possible subsets in which player i could be included. Shapley values satisfy four key axioms: *linearity, dummy player, symmetry*, and *efficiency* (Young, 1985). These axioms ensure a fair and consistent distribution of the total reward among all players.

3.2 Model-Based Estimation of Shapley Values

Calculating Shapley values to explain individual predictions presents substantial computational challenges (Chen et al., 2023a). To mitigate this burden, these values are typically approximated using sampling-based estimators, such as those in (Lundberg, 2017; Covert & Lee, 2020), though the sampling cost remains considerable. Recently, a more efficient model-based approach, introduced in (Jethani et al., 2021), accelerates the approximation by training a proxy explainer to compute Shapley values through a single model inference. However, this method has not been validated on advanced neural architectures such as transformers.

Building on this, ViT Shapley (Covert et al., 2022) was introduced to train a ViT explainer that interprets a pre-trained ViT model f. As shown in Figure 3(a), the learning process of the explainer consists of two stages. In stage 1, a surrogate model g_β with parameters β is generated by fine-tuning the pre-trained ViT classifier f to handle partial information, which is used for calculating the masked variables in the Shapley value. This involves aligning the output distributions of the surrogate model g_β with the classifier f. The surrogate is optimized with the following objective:

$$\mathcal{L}_{\text{surr}}(\beta) = \mathop{\mathbb{E}}_{x \sim p(x), s \sim \mathcal{U}(0,d)} \left[D_{\text{KL}} \left(f(x) \| g_\beta(x_s) \right) \right], \tag{2}$$

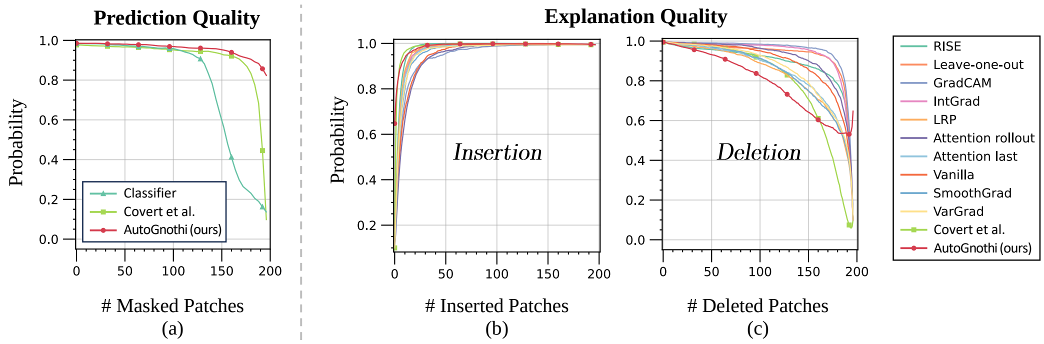

Figure 4: **Training performance of surrogate and explainer models.** (a) Prediction accuracy of masked inputs for the original classifier, the surrogate model trained with ViT Shapley (Covert et al., 2022), and our *AutoGnothi*. *AutoGnothi* shows greater robustness as the number of masked patches increases. For each mask size, we randomly sampled 100 images and generated 10 random masks. The curve represents the average prediction probability. (b) Explanation quality, measured by insertion and deletion metrics, for various explanation methods. We randomly sampled 1,000 images and averaged the prediction probabilities to assess insertion and deletion performance. All experiments were conducted on the ImageNette dataset using the ViT-base model.

where $\mathcal{U}(0, d)$ is a uniform distribution for sampling s. Then, in stage 2, an explainer ϕ_θ with parameters θ is trained to generate explanations of the predictions of the black-box ViT f, utilizing the surrogate model g_β. This optimization method was first proposed by (Charnes et al., 1988) and later applied in (Lundberg, 2017; Jethani et al., 2021; Covert et al., 2022). Let $p(x)$ and $p(x, y)$ denote the distributions of input and input-label pairs, respectively. Specifically, the loss for training the explainer is:

$$\mathcal{L}_{\text{exp}}(\theta) = \mathop{\mathbb{E}}_{(x,y)\sim p(x,y), s\sim q(s)} \left[\left(g_\beta(x_s|y) - g_\beta(x_{\mathbf{0}}|y) - s^\top \phi_\theta(x, y) \right)^2 \right] \tag{3}$$

$$\text{s.t.} \quad \mathbf{1}^\top \phi_\theta(x, y) = g_\beta(x_{\mathbf{1}}|y) - g_\beta(x_{\mathbf{0}}|y) \quad \forall (x, y), \tag{Efficiency}$$

where the constraint in the loss function is enforced to satisfy the efficiency axiom of the Shapley value, and $q(s)$ is defined with the Shapley kernel (Charnes et al., 1988) as follows:

$$q(s) \propto \frac{d-1}{\binom{d}{\mathbf{1}^\top s}(\mathbf{1}^\top s)(d - \mathbf{1}^\top s)} \quad \forall s : 0 < \mathbf{1}^\top s < d, \tag{Shapley Kernel}$$

In addition, the ViT explainer ϕ_θ has the same number of multi-head self-attention (MSA) layers as the feature backbone, and includes three additional MSA layers and a fully-connected (FC) layer as the explanation head. By learning the explainer ϕ_θ to estimate Shapley values, the computational cost is reduced to a constant complexity of $\mathcal{O}(1)$.

4 Method

4.1 Efficiently Training the Shapley Value Explainer for Black-Box Models

As discussed in Section 3.2, existing methods for approximating Shapley values require two stages. First, the black-box model f is fully fine-tuned to obtain a surrogate model g with the same trainable parameters and memory cost as f. Then, an explainer ϕ is fully trained using g. These stages at least double the training, memory, and inference costs compared to using the black-box model f alone, making these methods impractical for large models.

To improve training, memory, and inference efficiency, we propose a side-tuning pipeline called *AutoGnothi*, as shown in Figure 3(b). Building on ideas from PETL, we adapt Ladder Side-Tuning (LST) (Sung et al., 2022) by incorporating an additive side network. This side network separates the trainable parameters from the backbone model f and adapts the model to a different task. It is a lightweight version of f, with weights and hidden state dimensions scaled by a factor of $1/r$, where r is a reduction factor (*e.g.*, $r = 4$ or 8). For instance, if the backbone f has a 768-dimensional hidden state, then with $r = 8$, the side network has a hidden state dimension of 96. By computing gradients solely for the side network, this design avoids a backward pass through the

Table 1: Comparison of training and memory efficiency across different models. We evaluated memory consumption and trainable parameters for previous methods (Covert et al., 2022) and *AutoGnothi* across a range of models and tasks. For surrogate models, we measured classification accuracy, while for explainers, we assessed explanation quality using insertion and deletion metrics. It is important to note that prediction accuracy for the classifier is evaluated on normal inputs, whereas for the surrogate model, accuracy is measured on masked inputs.

Dataset		ImageNette				MURA	Pet	Yelp
Model		ViT-T	ViT-S	ViT-B	ViT-L	ViT-B	ViT-B	BERT-B
Classifier to be explained	Memory (MB)	84.90	331.80	1311.61	4631.25	1311.50	1311.93	1676.59
	#Params (M)	5.53	21.67	85.81	303.31	85.80	85.83	109.48
	Accuracy (↑)	0.9791	0.9944	0.9944	0.9964	0.8186	0.9469	0.9010
Surrogate (Covert et al.)	Memory (MB)	84.90	331.80	1311.61	4631.25	1311.50	1311.93	1676.59
	#Params (M)	5.53	21.67	85.81	303.31	85.80	85.83	109.48
	Accuracy (↑)	0.9822	0.9934	0.9939	0.9975	0.8233	0.9469	0.9490
Surrogate (*AutoGnothi*)	Memory (MB)	23.83 (-72%)	92.38 (-72%)	363.64 (-72%)	1280.80 (-72%)	438.10 (-67%)	363.76 (-72%)	532.71 (-68%)
	#Params (M)	0.14 (-97%)	0.56 (-97%)	2.23 (-97%)	7.91 (-97%)	7.11 (-92%)	2.23 (-97%)	7.15 (-93%)
	Accuracy (↑)	0.9791	0.9939	0.9959	0.9959	0.8139	0.9422	0.9280
Explainer (Covert et al.)	Memory (MB)	103.05	404.10	1600.21	5144.05	1599.79	1601.47	1955.87
	#Params (M)	6.72	26.41	104.72	336.92	104.69	104.80	127.79
	Insertion (↑)	0.9824	0.9828	0.9839	0.9843	0.9319	0.9422	0.9620
	Deletion (↓)	0.5243	0.6865	0.8121	0.7646	0.4199	0.4958	0.1725
Explainer (*AutoGnothi*)	Memory (MB)	24.02 (-77%)	93.12 (-77%)	366.51 (-77%)	1285.87 (-75%)	449.38 (-72%)	366.75 (-77%)	685.32 (-65%)
	#Params (M)	0.15 (-98%)	0.61 (-98%)	2.42 (-98%)	8.24 (-98%)	7.85 (-93%)	2.43 (-98%)	17.15 (-87%)
	Insertion (↑)	0.9802	0.9791	0.9874	0.9837	0.9292	0.9384	0.9588
	Deletion (↓)	0.5097	0.6667	0.7954	0.6570	0.4116	0.4888	0.1004

main backbone, improving training and memory efficiency. The formulation combines the frozen pre-trained backbone and the side-tuner with learnable parameters β as:

$$y^{\text{main}} = \underbrace{f}_{\text{frozen}}(x), \quad y^{\text{surr}} = \underbrace{g_\beta}_{\text{trainable}}(x_s), \quad \phi^{\text{exp}} = \underbrace{\phi_\theta}_{\text{trainable}}(x), \tag{4}$$

where g_β is trained by minimizing the loss in Eq.(2), and ϕ_θ is trained by minimizing the loss in Eq.(3), respectively.

4.1.1 Obtaining the Surrogate

To obtain the surrogate model, *AutoGnothi* applies LST directly to the black-box model f, utilizing the additive side branch g with parameters β to predict the masked inputs x_s of sample x. Let $f^{(i)}$ and $g^{(i)}$ denote the i-th MSA block of the main model f and the surrogate branch g, respectively. Assume there are N MSA blocks in total. Let z_1^{main} denote the output for masked input x_s of the first MSA layer $f^{(1)}$ of f, *i.e.*, $z_1^{\text{main}} = f^{(1)}(x_s)$. The forward process of the frozen main model f with the side-tuning branch g is:

$$z_i^{\text{main}} = f^{(i)}(z_{i-1}^{\text{main}}), \quad z_i^{\text{surr}} = g^{(i)}(\text{FC}^{(i)}(z_i^{\text{main}})). \tag{5}$$

After N MSA blocks, an FC head is applied to generate the prediction for the partial information, *i.e.*, $y^{\text{surr}} = \text{FC}_{\text{head}}(z_N^{\text{surr}})$). The convergence of the surrogate model is analyzed as follows:

Theorem 1 (Proof in Appendix B)**.** *Let the surrogate model be trained using gradient descent with step size α for t iterations. The expected KL divergence between the original model's predictions $f(x)$ and the surrogate model's predictions $g_\beta(x_s)$ is upper-bounded by:*

$$\mathbb{E}_{x\sim p(x), s\sim\mathcal{U}(0,d)}\left[D_{KL}\left(f(x)\|g_\beta(x_s)\right)\right] \leq \frac{1}{2\mu}(1-\mu\alpha)^t\left(\mathcal{L}_{surr}(\beta_0) - \mathcal{L}^\star_{surr}\right), \tag{6}$$

where β_0 is the initial parameter value, $\mathcal{L}^\star_{surr}$ is the optimal value during optimization, and μ is the minimal eigenvalue of the Hessian of $\mathcal{L}_{surr}$.

Theorem 1 establishes a theoretical guarantee that a side-tuned surrogate can achieve performance comparable to that of a fully trained surrogate. The detailed proof is provided in Appendix B.

Figure 3(b) shows the pipeline of obtaining the surrogate in stage 1. An intuitive performance comparison of prediction models is presented in Figure 4(a). *AutoGnothi*'s surrogate surpasses the original classifier in terms of prediction accuracy and matches the performance of (Covert et al., 2022) when handling partial information, but with only 3% trainable parameters. Additionally, *AutoGnothi*'s surrogate exhibits more robust predictions as the number of masked inputs increases. A detailed comparison of the training and memory costs on different models is provided in Table 1.

Table 2: Inference efficiency comparison of various models. We assessed the computational cost (FLOPs), total parameters, and inference time for different methods. For the baseline method (Covert et al., 2022), we calculated these values separately for the classifier and explainer, and then combined them. In contrast, for *AutoGnothi*, we computed these values directly from our self-interpretable models, who can generate both predictions and explanations simultaneously.

Dataset		ImageNette				MURA	Pet	Yelp
Model		ViT-T	ViT-S	ViT-B	ViT-L	ViT-B	ViT-B	BERT-B
Classifier + Explainer (Covert et al.)	FLOPs (G)	4.78	18.86	74.90	251.96	74.88	74.93	213.51
	Time (ms)	19.7	39.0	94.9	310.3	100.3	100.2	166.90
	#Params (M)	12.25	48.08	190.53	640.23	190.49	190.63	237.27
Self-Interpretable Model (*AutoGnothi*)	FLOPs (G)	2.22 (-54%)	8.73 (-54%)	34.67 (-54%)	122.60 (-51%)	36.81 (-51%)	34.67 (-54%)	116.66 (-45%)
	Time (ms)	15.4 (-22%)	23.0 (-41%)	52.9 (-44%)	179.1 (-42%)	56.7 (-43%)	57.0 (-43%)	118.55 (-29%)
	#Params (M)	5.68 (-54%)	22.28 (-54%)	88.22 (-54%)	311.55 (-51%)	93.65 (-51%)	88.25 (-54%)	126.63 (-47%)

4.1.2 Obtaining the Explainer

For the explainer model, *AutoGnothi* uses a similar LST feature backbone as in the surrogate model g, consisting of N MSA blocks for feature extraction. Let $\phi^{(i)}$ represent the i-th MSA block of the explainer branch ϕ. In addition to the lightweight backbone blocks in the side branch, we add M extra FC layers as the explanation head. Together, the side network ϕ generates explanations based on the backbone features from the main branch. Let z_1^{main} denote the output for input x from the first MSA layer $f^{(i)}$ of the main branch f, *i.e.*, $z_1^{\text{main}} = f^{(1)}(x)$. The forward process of the explainer is:

$$
\begin{aligned}
z_i^{\text{main}} = f^{(i)}(z_{i-1}^{\text{main}}), \quad z_i^{\text{exp}} = \phi^{(i)}(\text{FC}^{(i)}(z_i^{\text{main}})) \quad \forall i \in \{1, \dots, N\}, \\
\phi^{\text{exp}}(x) = \text{FC}_{\text{head}}^{(M)}\left(\text{FC}_{\text{head}}^{(M-1)}\left(\dots\left(\text{FC}_{\text{head}}^{(1)}\left(z_N^{\text{exp}}\right)\right)\right)\right),
\end{aligned} \tag{7}
$$

where the main branch f remains uncontaminated. We provide a theoretical guarantee for the convergence of the trained side branch ϕ as follows:

Theorem 2 (Proof in Appendix B)**.** *Let $\phi_v(x|y)$ denote the exact Shapley value for input-output pair (x, y) in game v. The expected regression loss $\mathcal{L}_{exp}(\theta)$ upper bounds the Shapley value estimation error as follows,*

$$
\mathbb{E}_{p(x,y)}\left[\left|\left|\phi_\theta(x, y) - \phi_v(x|y))\right|\right|_2\right] \le \sqrt{2H_{d-1}\left(\mathcal{L}_{exp}(\theta) - \mathcal{L}_{exp}^{\star}\right)}, \tag{8}
$$

where $\mathcal{L}_{exp}^{\star}$ represents the optimal loss achieved by the exact Shapley values, and H_{d-1} is the $(d-1)$-th harmonic number.

Theorem 2 provides a theoretical guarantee that a side-tuned explainer can achieve performance on par with a fully trained explainer. The complete proof is presented in Appendix B.

Figure 3(b) shows the pipeline of obtaining the explainer in stage 2. We evaluated the explanation quality of *AutoGnothi* against various baselines, as shown in Figure 4(b). *AutoGnothi* achieved the highest insertion and lowest deletion scores among 12 explanation methods, demonstrating superior explanation quality. Compared to (Covert et al., 2022), we reduced the trainable parameters for explainers by 98% while maintaining comparable or even superior interpretability. Table 1 provides detailed comparisons of training and memory efficiency for different models.

4.1.3 Generating Explanation for Black-Box Models

After obtaining the explainer, we now detail the explanation procedure. In most post-hoc explanation methods (Selvaraju et al., 2020; Chattopadhay et al., 2018; Binder et al., 2016; Covert et al., 2022), predictions and explanations must be computed separately for a single input. For instance, as illustrated in Figure 3(a), two separate inferences are required to explain a single prediction. In contrast, as shown in Figure 3(b), *AutoGnothi* generates both predictions and explanations simultaneously, needing only one inference. To evaluate this efficiency, we measured inference time, computational cost (FLOPs), and total parameters required to generate predictions and explanations for different methods. The comparison of inference efficiency is highlighted in Table 2.

4.2 Difference between *AutoGnothi* and previous PETL Methods

In this section, we provide an empirical analysis of why *AutoGnothi* outperforms previous PETL approaches. We highlight that *AutoGnothi* is not a simple extension of classical PETL, where full fine-tuning is typically the optimal baseline. Additionally, *AutoGnothi* exploits the intrinsic correlation between the prediction task and its explanation, enabling black-box models to become self-interpretable without sacrificing prediction accuracy. We elaborate on these two points below.

Full fine-tuning poses challenges for achieving self-interpretability and is not the optimal baseline for *AutoGnothi*. For classical PETL, the goal is often to match the performance of fully fine-tuned models on standard tasks (Houlsby et al., 2019; Chen et al., 2023b; Hu et al., 2021; Mercea et al., 2024). However, in XAI scenarios, the challenge shifts: it becomes difficult, if not impossible, to train a model that balances both prediction accuracy and explanation quality (Arrieta et al., 2020; Gunning et al., 2019; Došilović et al., 2018). In fact, fine-tuning models to adapt interpretability without forgetting pre-trained knowledge can be difficult (Li & Hoiem, 2017). Additionally, full fine-tuning the original model also puts us in the *Theseus's Paradox*: we won't be sure if we are explaining the very same model anymore. Even if full fine-tuning were practical, it would contradict the goal of interpreting the pre-trained model. In contrast, *AutoGnothi* pipeline addresses this issue by freezing the primary model and training only a side network to generate explanations, offering an efficient solution that enables self-interpretability without degrading prediction performance.

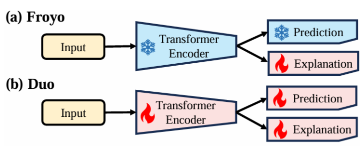

(c)

Method	Accuracy (%)	Insertion (↑)	Deletion (↓)
AutoGnothi	**99.44**	**0.9874**	**0.7954**
Covert et al.	**99.44**	0.9839 (-0.003)	0.8121 (+0.017)
Froyo	**99.44**	0.9493 (-0.038)	0.9365 (+0.141)
Duo	95.46 (-4%)	0.9460 (-0.041)	0.9375 (+0.142)

Figure 5: Other pipelines to achieve the self-interpretability through the full fine-tuning. (a) Freeze the transformer encoder and prediction head, learning only the explanation head. (b) Simultaneously learn the transformer encoder, and both task heads. (c) Comparison of classification and explanation performance between different pipelines for ViT-base.

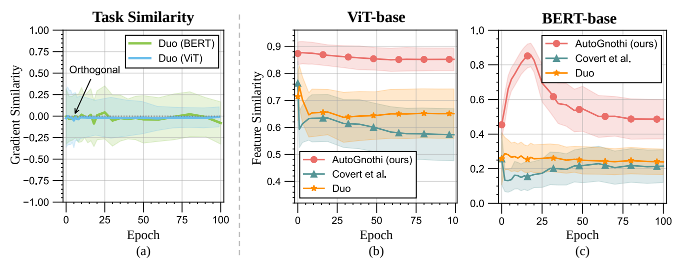

Figure 6: Explanation of why the Duo pipeline underperforms compared to *AutoGnothi*. (a) The full fine-tuning strategy employed by Duo is not the optimal baseline for *AutoGnothi* due to significant gradient conflicts between the prediction and explanation tasks. This conflict results in degraded performance, raising concerns about whether the explanation truly pertains to the same model. Note that gradient similarity can only be measured for the Duo pipeline, as other methods freeze the prediction backbones. (b) In contrast, *AutoGnothi* exhibits a stronger correlation between features of the prediction and explanation tasks. We measured the feature similarity with CKA.

Building on prior work that highlights the challenges of achieving self-interpretability through full fine-tuning, we conducted experiments to further explore this issue. As depicted in Figure 5(a)(b), we introduce two additional pipelines, *Froyo* and *Duo*. *Froyo* adds an explanation head while keeping the transformer encoder and prediction head frozen to preserve prediction accuracy. In contrast, *Duo* jointly learns both the prediction task and its explanation. Both pipelines use the same encoder, prediction head, and explanation head architectures as described in (Covert et al., 2022).

We performed experiments using ViT-base model trained on the ImageNette dataset. Our findings show that the *Froyo* pipeline underperforms due to the limited trainable parameters in the explanation head, resulting in degraded explanation quality. As illustrated in Figure 5(c), this led to a reduction in insertion by 0.038 and an increase in deletion by 0.141, despite no impact on prediction accuracy.

For the Duo pipeline, we observed a 4.0% decline in prediction accuracy on the ViT-base model, accompanied by a reduction in insertion by 0.041 and an increase in deletion by 0.142. Further empirical evidence, as depicted in Figure 6(a), highlights conflicting gradients between the prediction and explanation tasks during training. Additionally, as previously discussed, the *Theseus's Paradox* arises when changes in predictions result in evolving explanations, thereby challenging the consistency and identity of the original model.

***AutoGnothi* uncovers the intrinsic correlation between predictions and explanations.** While the *AutoGnothi* pipeline enables self-interpretation with superior efficiency, the underlying mechanisms connecting prediction and explanation remain underexplored. We propose that *AutoGnothi* leverages the intrinsic relationship between the backbone features used for both tasks. This correlation is illustrated in Figure 6(b), where we evaluated the Central Kernel Alignment (CKA) (Kornblith et al., 2019) between the backbone features of the original pre-trained model and those of various explainers. Our results show that *AutoGnothi* exhibits higher feature similarity between prediction and explanation tasks on ViT-base and BERT-base models, supporting our hypothesis.

5 Experiments

5.1 Experimental Settings

Datasets and Black-box Models. For image classification, we used the ImageNette (Howard & Gugger, 2020), Oxford IIIT-Pets (Parkhi et al., 2012), and MURA (Rajpurkar et al., 2017) datasets, following (Covert et al., 2022). For sentiment analysis, we utilized the Yelp Review Polarity dataset (Zhang et al., 2015). In terms of black-box models, we employed the widely used ViT models (Dosovitskiy, 2020) for vision tasks, including ViT-tiny, ViT-small, ViT-base, and ViT-large. For language tasks, we used the BERT-base model (Devlin et al., 2019).

Implementation Details. For surrogates and explainers, *AutoGnothi* incorporates the same number of MSA blocks as the black-box model being explained in the side network and utilizes a reduction factor of $r = 8$ for the lightweight side branch on both the ImageNette and Oxford IIIT-Pets datasets, and $r = 4$ for MURA and Yelp Review Polarity. Surrogates use the same task head as the black-box classifiers with one additional FC layer as classification head for handling partial information. Explainers utilize three additional FC layers as the explanation head after the side network backbone. For attention masking, we employed a causal attention masking strategy, setting attention values to a large negative number before applying the softmax operation (Brown, 2020). More detailed training settings are provided in Appendix A.

Table 3: Quality metrics (insertion and deletion) for target class explanations of ViT-base across baseline methods and *AutoGnothi* on the ImageNette dataset. More results for other datasets and models are provided in Appendix E.

Method	Insertion (↑)	Deletion (↓)
Random	0.9578$\pm$0.0790	0.9584$\pm$0.0764
Attention last	0.9633$\pm$0.0659	0.8524$\pm$0.1748
Attention rollout	0.9408$\pm$0.0834	0.9168$\pm$0.1277
GradCAM (Attn)	0.9447$\pm$0.0936	0.9562$\pm$0.0916
GradCAM (LN)	0.9343$\pm$0.0829	0.9426$\pm$0.1307
Vanilla (Pixel)	0.9487$\pm$0.0688	0.8945$\pm$0.1513
Vanilla (Embed)	0.9563$\pm$0.0643	0.8618$\pm$0.1754
IntGrad (Pixel)	0.9670$\pm$0.0575	0.9408$\pm$0.1141
IntGrad (Embed)	0.9670$\pm$0.0575	0.9408$\pm$0.1141
SmoothGrad (Pixel)	0.9591$\pm$0.0760	0.8459$\pm$0.1788
SmoothGrad (Embed)	0.9529$\pm$0.0931	0.9561$\pm$0.0764
VarGrad (Pixel)	0.9616$\pm$0.0725	0.8600$\pm$0.1692
VarGrad (Embed)	0.9552$\pm$0.0901	0.9568$\pm$0.0756
LRP	0.9677$\pm$0.0623	0.8393$\pm$0.1866
Leave-one-out	0.9696$\pm$0.0353	0.9334$\pm$0.1493
RISE	0.9772$\pm$0.0225	0.8959$\pm$0.1962
Covert et al.	0.9839$\pm$0.0375	0.8121$\pm$0.1768
AutoGnothi (Ours)	**0.9874$\pm$0.0265**	**0.7954$\pm$0.2294**

Evaluation Metrics for Explanations. We used the widely adopted insertion and deletion metrics (Petsiuk, 2018) to evaluate explanation quality. These metrics are computed by progressively inserting or deleting features based on their importance and observing the impact on the model's predictions. The corresponding surrogate model trained to handle partial inputs is used for this process to generate prediction for masked inputs. We calculated the area under the curve (AUC) for the predictions and average results for randomly selected $1,000$ samples on all datasets.

Baseline Methods. We considered 12 representative explanation methods for comparison. For attention-based methods, we utilized attention rollout and attention last (Abnar & Zuidema, 2020). For gradient-based methods, we used Vanilla Gradients (Simonyan, 2013), IntGrad (Sundararajan et al., 2017), SmoothGrad (Smilkov et al., 2017), VarGrad (Hooker et al., 2019), LRP (Binder et al., 2016), and GradCAM (Selvaraju et al., 2020). For removal-based methods, we employed leave-one-out (Zeiler & Fergus, 2014) and RISE (Petsiuk, 2018). For Shapley value-based methods, we utilized KernelSHAP (Lundberg, 2017) and ViT Shapley (Covert et al., 2022) as baselines.

5.2 Evaluating Training, Memory and Inference Efficiency

To evaluate the training and memory efficiency of *AutoGnothi*, we compared it with various baselines in terms of trainable parameters and memory usage. Table 1 provides a summary of the memory

Figure 7: Visualization of ViT explanations on the ImageNette, Oxford-IIIT Pets, and MURA datasets. *AutoGnothi* qualitatively outperforms other baseline approaches.

costs and trainable parameters for both surrogate and explainer models across different methods. During training, *AutoGnothi* achieves a significant reduction of over 87% in trainable parameters and more than 65% in GPU memory usage for both surrogates and explainers on both vision and language datasets, while maintaining competitive performance in both prediction accuracy and explanation quality. The memory cost is evaluated with training batch size $= 1$.

Next, we evaluate the inference efficiency of our self-interpretable models by comparing the computational cost (FLOPs), inference time, and the total number of parameters required for generating both predictions and explanations. As shown in Table 2, *AutoGnothi* significantly reduces inference time and FLOPs compared to baseline models that require separate inferences for predictions and explanations. Specifically, when both the predictions and the explanations are required, *AutoGnothi* is capable of reducing at least 45% in FLOPs, 22% in inference time (up to 44%), and 47% in total parameters end-to-end across all datasets and tasks.

5.3 Evaluating Explanation Quality

Quantitative Results. To evaluate the quality of explanations generated by *AutoGnothi*, we compared it against 12 state-of-the-art baseline methods using the insertion and deletion metrics. Table 3 presents results from a ViT-base model trained on the ImageNette dataset, where *AutoGnothi* consistently achieves the best insertion and deletion scores for target class explanations across various datasets. Further detailed results for other models and tasks are provided in Appendix E. For vision task, please refer to Tables 5, 6, and 7 for the results of ViT-tiny, ViT-small, and ViT-large on ImageNette, respectively. Results for ViT-base on Oxford-IIIT Pets are provided in Table 8, and results for ViT-base on Mura are shown in Table 9. For language task, we also provide results of BERT-base on Yelp Reivew Polarity in Table 10.

Qualitative Results. We also provide visualization results for ViTs on different datasets, as shown in Figure 7. It may be observed that RISE happened to fail to provide human-interpretable or intuitive results, which amongst all others *AutoGnothi* offers more accurate explanations with a clearer focus on the subject and diluted colours for irrelevant classes. Additional visualization results for ViT-base on more datasets are provided in Appendix J, shown in Figures 17, 18, 19, 20, 21, and 22.

6 Conclusion

This paper introduces *AutoGnothi* to bridge the gap between self-interpretable models and post-hoc explanation methods in Explainable AI. Inspired by parameter-efficient transfer-learning, *AutoGnothi* incorporates a lightweight side network that allows black-box models to generate faithful Shapley value explanations without affecting the original predictions. Notably, *AutoGnothi* outperforms directly fine-tuning the all the parameters in the model for explanation by a clear margin. This approach empowers black-box models with self-interpretability, which is superior to standard post-hoc explanations that require generating predictions and explanations in two separate, heavy inferences. Experiments on ViT and BERT demonstrate that *AutoGnothi* achieves superior efficiency on computation, storage and memory in both training and inference periods.

REFERENCES

Samira Abnar and Willem Zuidema. Quantifying attention flow in transformers. In *Proceedings of the 58th Annual Meeting of the Association for Computational Linguistics*, pp. 4190–4197, 2020.

Josh Achiam, Steven Adler, Sandhini Agarwal, Lama Ahmad, Ilge Akkaya, Florencia Leoni Aleman, Diogo Almeida, Janko Altenschmidt, Sam Altman, Shyamal Anadkat, et al. Gpt-4 technical report. *arXiv preprint arXiv:2303.08774*, 2023.

David Alvarez-Melis and Tommi S. Jaakkola. Towards robust interpretability with self-explaining neural networks, 2018.

Alejandro Barredo Arrieta, Natalia Díaz-Rodríguez, Javier Del Ser, Adrien Bennetot, Siham Tabik, Alberto Barbado, Salvador García, Sergio Gil-López, Daniel Molina, Richard Benjamins, et al. Explainable artificial intelligence (xai): Concepts, taxonomies, opportunities and challenges toward responsible ai. *Information fusion*, 58:82–115, 2020.

Alexander Binder, Grégoire Montavon, Sebastian Lapuschkin, Klaus-Robert Müller, and Wojciech Samek. Layer-wise relevance propagation for neural networks with local renormalization layers. In *Artificial Neural Networks and Machine Learning–ICANN 2016: 25th International Conference on Artificial Neural Networks, Barcelona, Spain, September 6-9, 2016, Proceedings, Part II 25*, pp. 63–71. Springer, 2016.

Samuel R Bowman, Gabor Angeli, Christopher Potts, and Christopher D Manning. A large annotated corpus for learning natural language inference. *arXiv preprint arXiv:1508.05326*, 2015.

Tom B Brown. Language models are few-shot learners. *arXiv preprint arXiv:2005.14165*, 2020.

A. Charnes, B. Golany, M. Keane, and J. Rousseau. *Extremal Principle Solutions of Games in Characteristic Function Form: Core, Chebychev and Shapley Value Generalizations*, pp. 123–133. Springer Netherlands, Dordrecht, 1988. ISBN 978-94-009-3677-5.

Aditya Chattopadhay, Anirban Sarkar, Prantik Howlader, and Vineeth N Balasubramanian. Grad-cam++: Generalized gradient-based visual explanations for deep convolutional networks. In *2018 IEEE winter conference on applications of computer vision (WACV)*, pp. 839–847. IEEE, 2018.

Hugh Chen, Ian C Covert, Scott M Lundberg, and Su-In Lee. Algorithms to estimate shapley value feature attributions. *Nature Machine Intelligence*, 5(6):590–601, 2023a.

Zhe Chen, Yuchen Duan, Wenhai Wang, Junjun He, Tong Lu, Jifeng Dai, and Yu Qiao. Vision Transformer Adapter for Dense Predictions (ViT-Adapter), February 2023b. arXiv:2205.08534 [cs] Read_Status: In Progress Read_Status_Date: 2024-07-11T08:26:12.114Z.

Christopher Clark, Kenton Lee, Ming-Wei Chang, Tom Kwiatkowski, Michael Collins, and Kristina Toutanova. Boolq: Exploring the surprising difficulty of natural yes/no questions. *arXiv preprint arXiv:1905.10044*, 2019.

Julien Colin, Thomas Fel, Rémi Cadène, and Thomas Serre. What i cannot predict, i do not understand: A human-centered evaluation framework for explainability methods. *Advances in neural information processing systems*, 35:2832–2845, 2022.

Ian Covert and Su-In Lee. Improving kernelshap: Practical shapley value estimation via linear regression. *arXiv preprint arXiv:2012.01536*, 2020.

Ian Covert, Chanwoo Kim, and Su-In Lee. Learning to estimate shapley values with vision transformers. *arXiv preprint arXiv:2206.05282*, 2022.

Jacob Devlin, Ming-Wei Chang, Kenton Lee, and Kristina Toutanova. Bert: Pre-training of deep bidirectional transformers for language understanding. In *North American Chapter of the Association for Computational Linguistics*, 2019.

Filip Karlo Došilović, Mario Brčić, and Nikica Hlupić. Explainable artificial intelligence: A survey. In *2018 41st International convention on information and communication technology, electronics and microelectronics (MIPRO)*, pp. 0210–0215. IEEE, 2018.

Alexey Dosovitskiy. An image is worth 16x16 words: Transformers for image recognition at scale. *arXiv preprint arXiv:2010.11929*, 2020.

David Gunning, Mark Stefik, Jaesik Choi, Timothy Miller, Simone Stumpf, and Guang-Zhong Yang. Xai—explainable artificial intelligence. *Science robotics*, 4(37):eaay7120, 2019.

Dan Hendrycks and Thomas Dietterich. Benchmarking neural network robustness to common corruptions and perturbations. *arXiv preprint arXiv:1903.12261*, 2019.

Dan Hendrycks and Kevin Gimpel. Bridging nonlinearities and stochastic regularizers with gaussian error linear units, 2017.

Sara Hooker, Dumitru Erhan, Pieter-Jan Kindermans, and Been Kim. A benchmark for interpretability methods in deep neural networks. *Advances in neural information processing systems*, 32, 2019.

Neil Houlsby, Andrei Giurgiu, Stanislaw Jastrzebski, Bruna Morrone, Quentin De Laroussilhe, Andrea Gesmundo, Mona Attariyan, and Sylvain Gelly. Parameter-efficient transfer learning for nlp. In *International conference on machine learning*, pp. 2790–2799. PMLR, 2019.

Jeremy Howard and Sylvain Gugger. Fastai: a layered api for deep learning. *Information*, 11(2): 108, 2020.

Edward J. Hu, Yelong Shen, Phillip Wallis, Zeyuan Allen-Zhu, Yuanzhi Li, Shean Wang, Lu Wang, and Weizhu Chen. LoRA: Low-Rank Adaptation of Large Language Models, October 2021. arXiv:2106.09685 [cs] Read_Status: Read Read_Status_Date: 2024-07-11T07:26:20.161Z.

Neil Jethani, Mukund Sudarshan, Ian Connick Covert, Su-In Lee, and Rajesh Ranganath. Fastshap: Real-time shapley value estimation. In *International conference on learning representations*, 2021.

Been Kim, Martin Wattenberg, Justin Gilmer, Carrie Cai, James Wexler, Fernanda Viegas, et al. Interpretability beyond feature attribution: Quantitative testing with concept activation vectors (tcav). In *International conference on machine learning*, pp. 2668–2677. PMLR, 2018.

Alexander Kirillov, Eric Mintun, Nikhila Ravi, Hanzi Mao, Chloe Rolland, Laura Gustafson, Tete Xiao, Spencer Whitehead, Alexander C Berg, Wan-Yen Lo, et al. Segment anything. In *Proceedings of the IEEE/CVF International Conference on Computer Vision*, pp. 4015–4026, 2023.

Pang Wei Koh, Thao Nguyen, Yew Siang Tang, Stephen Mussmann, Emma Pierson, Been Kim, and Percy Liang. Concept bottleneck models. In *International conference on machine learning*, pp. 5338–5348. PMLR, 2020.

Simon Kornblith, Mohammad Norouzi, Honglak Lee, and Geoffrey Hinton. Similarity of neural network representations revisited. In *International conference on machine learning*, pp. 3519–3529. PMLR, 2019.

Zhizhong Li and Derek Hoiem. Learning without forgetting. *IEEE transactions on pattern analysis and machine intelligence*, 40(12):2935–2947, 2017.

Yue Liu, Christos Matsoukas, Fredrik Strand, Hossein Azizpour, and Kevin Smith. Patchdropout: Economizing vision transformers using patch dropout. *arXiv preprint arXiv:2208.07220*, 2022.

Scott Lundberg. A unified approach to interpreting model predictions. *arXiv preprint arXiv:1705.07874*, 2017.

Andrew Maas, Raymond E Daly, Peter T Pham, Dan Huang, Andrew Y Ng, and Christopher Potts. Learning word vectors for sentiment analysis. In *Proceedings of the 49th annual meeting of the association for computational linguistics: Human language technologies*, pp. 142–150, 2011.

Aleksander Madry. Towards deep learning models resistant to adversarial attacks. *arXiv preprint arXiv:1706.06083*, 2017.

Otniel-Bogdan Mercea, Alexey Gritsenko, Cordelia Schmid, and Anurag Arnab. Time-, Memory- and Parameter-Efficient Visual Adaptation (LoSA), February 2024. arXiv:2402.02887 [cs].

Omkar M. Parkhi, Andrea Vedaldi, Andrew Zisserman, and C. V. Jawahar. Cats and dogs. In *IEEE Conference on Computer Vision and Pattern Recognition*, 2012.

V Petsiuk. Rise: Randomized input sampling for explanation of black-box models. *arXiv preprint arXiv:1806.07421*, 2018.

Alec Radford, Jong Wook Kim, Chris Hallacy, Aditya Ramesh, Gabriel Goh, Sandhini Agarwal, Girish Sastry, Amanda Askell, Pamela Mishkin, Jack Clark, et al. Learning transferable visual models from natural language supervision. In *International conference on machine learning*, pp. 8748–8763. PMLR, 2021.

Pranav Rajpurkar, Jeremy Irvin, Aarti Bagul, Daisy Ding, Tony Duan, Hershel Mehta, Brandon Yang, Kaylie Zhu, Dillon Laird, Robyn L Ball, et al. Mura: Large dataset for abnormality detection in musculoskeletal radiographs. *arXiv preprint arXiv:1712.06957*, 2017.

Cynthia Rudin. Stop explaining black box machine learning models for high stakes decisions and use interpretable models instead. *Nature machine intelligence*, 1(5):206–215, 2019.

Luis M. Ruiz, Federico Valenciano, and Jose M. Zarzuelo. The family of least square values for transferable utility games. *Games and Economic Behavior*, 24(1):109–130, 1998. ISSN 0899-8256. doi: https://doi.org/10.1006/game.1997.0622.

Ramprasaath R Selvaraju, Michael Cogswell, Abhishek Das, Ramakrishna Vedantam, Devi Parikh, and Dhruv Batra. Grad-cam: visual explanations from deep networks via gradient-based localization. *International journal of computer vision*, 128:336–359, 2020.

Lloyd S Shapley. A value for n-person games. *Contributions to the Theory of Games*, 2, 1953.

Grah Simon and Thouvenot Vincent. A projected stochastic gradient algorithm for estimating Shapley value applied in attribute importance. In *International Cross-Domain Conference for Machine Learning and Knowledge Extraction*, pp. 97–115. Springer, 2020.

Karen Simonyan. Deep inside convolutional networks: Visualising image classification models and saliency maps. *arXiv preprint arXiv:1312.6034*, 2013.

Daniel Smilkov, Nikhil Thorat, Been Kim, Fernanda Viégas, and Martin Wattenberg. Smoothgrad: removing noise by adding noise. *arXiv preprint arXiv:1706.03825*, 2017.

Mukund Sundararajan, Ankur Taly, and Qiqi Yan. Axiomatic attribution for deep networks. In *International conference on machine learning*, pp. 3319–3328. PMLR, 2017.

Yi-Lin Sung, Jaemin Cho, and Mohit Bansal. LST: Ladder Side-Tuning for Parameter and Memory Efficient Transfer Learning, October 2022. arXiv:2206.06522 [cs] Read_Status: Read Read_Status_Date: 2024-07-11T08:24:04.287Z.

C. Wah, S. Branson, P. Welinder, P. Perona, and S. Belongie. Technical Report CNS-TR-2011-001, California Institute of Technology, 2011.

H Peyton Young. Monotonic solutions of cooperative games. *International Journal of Game Theory*, 14(2):65–72, 1985.

Matthew D Zeiler and Rob Fergus. Visualizing and understanding convolutional networks. In *Computer Vision–ECCV 2014: 13th European Conference, Zurich, Switzerland, September 6-12, 2014, Proceedings, Part I 13*, pp. 818–833. Springer, 2014.

Jeffrey O. Zhang, Alexander Sax, Amir Zamir, Leonidas Guibas, and Jitendra Malik. Side-Tuning: A Baseline for Network Adaptation via Additive Side Networks, July 2020. arXiv:1912.13503 [cs] Read_Status: Read Read_Status_Date: 2024-07-11T07:26:14.074Z.

Xiang Zhang, Junbo Zhao, and Yann LeCun. Character-level Convolutional Networks for Text Classification. *arXiv:1509.01626 [cs]*, September 2015.

A FURTHER EXPERIMENTAL DETAILS

A.1 ENVIRONMENT

Our experiments were conducted on one 128-core AMD EPYC 9754 CPU with one NVIDIA GeForce RTX 4090 GPU with 24 GB VRAM. No multi-card training or inference was involved. We implemented the training and inference pipelines for image classification tasks under the PyTorch Lightning framework, and for the sentiment analysis task with just PyTorch. For evaluations on baseline methods we leverage the SHAP library (Lundberg, 2017), with minor modifications applied to bridge data format differences between Numpy and PyTorch.

A.2 FLOPS AND MEMORY

We used the `profile` function from the `thop` library to evaluate the FLOPs for each model during the inference stage. Memory consumption was manually calculated during the training stage based on the model parameters, activations, and intermediate results. Our memory estimations were made under the assumption that the memory was evaluated under a batch size of 1 and uses 32-bit floating point precision (torch.float32).

A.3 CLASSIFIER

The training of all tasks is split into 3 stages. In the first stage parameters of the classifier are inherited from the original base model verbatim, with the exception of *AutoGnothi* adding additional parameters for the new side branch, initialized with Kaiming initialization.

We fine-tune this classifier model on the exact same dataset with the AdamW optimizer, using a learning rate of 10^{-5} for 25 epochs, and retain the best checkpoint rated by minimal validation loss. Classification loss is minimum square error with respective to the predicted classes and the ground-truth labels. For *AutoGnothi* the classes come from the side branch, while all remaining models use the classes from the main branch. We train and evaluate these methods on 1 Nvidia RTX 4090, and use a batch size of 32 samples provided that it fits inside the available GPU memory.

We freeze parameters in all stages likewise. As is described in 4.2, *AutoGnothi* only trains the side branch and all parameters from the original model are frozen. In ViT-shapley (Covert et al.) and Duo pipelines, all parameters are trained, whilst the Froyo pipeline only trains the classification head.

A.4 SURROGATE

Surrogate models have the same model architecture as the classifiers, with a different recipe. We load all parameters from the classifier without any changes or additions, further fine-tune the model for 50 epochs, and retain the best checkpoint with minimal validation loss.

Unlike the classifier, the surrogate model focuses on mimicking the classifier model's behavior under a masked context. Consider the logits $p(y|x_{\mathbf{0}})$ from the classifier model, where x is the input and y is the corresponding class label. The surrogate model aims at closing in its masked logits distribution, $p(y|x_s)$, with the original distribution:

$$\mathcal{L}_{\text{surr}}(\beta) = \mathop{\mathbb{E}}_{x \sim p(x), s \sim \mathcal{U}(0,d)} \left[D_{\text{KL}} \left(f(x) \| g_\beta(x_s) \right) \right], \tag{1}$$

The mask is selected on an equi-categorical basis. We first pick an integer $n_s = s \cdot \mathbf{1}^\top$ at uniform distribution, denoting the number of tokens that shall be masked. n_s mutually exclusive indices are then randomly chosen from the input at uniform distribution. To avoid inhibiting model capabilities, special tokens like the implicit class token in ViT or the [CLS] token applied by the BERT tokenizer are never masked.

In order to selectively hide or mask inputs from the model, we apply causal attention masks for both the image models and text models in our experiments. However, it's worth noting that while they may confuse the transformer's attention mechanisms, certain other methods are also capable of concealing these input tokens, primarily zeroing or assigning random values to the said pixels in image models, or assigning [PAD] and [MASK] to the selected tokens. We follow prior work (Covert et al., 2022) and adhere to causal attention masks.

Recall that the transformer self-attention mechanism used in ViT (Dosovitskiy, 2020), BERT (Devlin et al., 2019). Given an attention input $t \in \mathbb{R}^{d \times h}$ and self-attention parameters $W_{\text{qkv}} \in \mathbb{R}^{h \times 3h'}$, whereas d is the number of tokens and h is the attention's hidden size, and h' be the size of each attention head, the output of the self-attention $\text{SA}(t)$ for a single head is computed as follows:

$$[Q, K, V] = u \cdot W_{\text{qkv}} \tag{2}$$

$$A = \text{softmax}\left(\frac{Q \cdot K^\top}{\sqrt{h'}}\right) \tag{3}$$

$$\text{SA}(t) = A \cdot V \tag{4}$$

Transformers in practice use a multiple k attention heads, holding that $k \cdot h' = h$. An attention projection matrix $P_{\text{msa}} \in \mathbb{R}^{h \times h}$ is used to combine the outputs of all attention heads. Denoting the i-th self-attention head's output as $SA_i(t)$, the final output of the attention layer $\text{MSA}(t)$ is thus computed:

$$\text{MSA}(t) = [\text{SA}_1(t), \text{SA}_2(t), \ldots, \text{SA}_n(t)] \cdot P_{\text{msa}} \tag{5}$$

We notice that the attention mechanism is entirely unrelated to the number of tokens, and can operate in the absence of certain input tokens. Let an indicator vector $s \in \{0, 1\}^d$ correspond to a subset of the input tokens (applying equally to images and text tokens), we calculate the masked self-attention over t and s as follows:

$$[Q, K, V] = u \cdot W_{Q,K,V} \tag{6}$$

$$A = \text{softmax}\left(\frac{Q \cdot K^\top - (1 - s) \cdot \infty}{\sqrt{h'}}\right) \tag{7}$$

$$\text{SA}(t, s) = A \cdot V \tag{8}$$

We apply masking to the multi-head attention layers likewise, such that:

$$\text{MSA}(t, s) = [\text{SA}_1(t, s), \text{SA}_2(t, s), \ldots, \text{SA}_n(t, s)] \cdot P_{\text{msa}} \tag{9}$$

This mechanism is widely implemented for attention models in commonplace libraries such as HuggingFace's Transformers, named by the argument `attention_mask` in the input tensor.

A.5 Explainer

We load explainer model parameters from surrogate model checkpoints, such that all are copied from the surrogate model to the explainer model, except for the last classification head, which is replaced with an explainer head. The explainer head contains 3 MLP layers and a final linear layer, with GeLU (Hendrycks & Gimpel, 2017) activations from in between. For *AutoGnothi* only the classification head on the side branch is replaced. We train the explainer model for 100 epochs with the AdamW optimizer, using a learning rate of 10^{-5}, and keep the best checkpoint.

In our implementation, we took 2 input images in each mini-batch and generated 16 random masks for each image, resulting in a parallelism of 32 instances per batch. A slight change is applied to the masking algorithm in the explainer model from the surrogate model, in order to reduce variance during gradient descent. Specifically, in addition to generating masks uniform, we follow prior work (Covert et al., 2022) and use the paired sampling trick (Covert & Lee, 2020), pairing each subset s with its complement $\mathbf{1} - s$. This algorithm equally applies to both image and text classification models.

The explainer model is trained to approximate the Shapley value $\phi_\theta(x, y)$. Let $g_\beta(x_s|y)$ be the surrogate values respective to the input x and the class y, masked by the indicator vector s, and

$g_\beta(x_{\mathbf{0}}|y)$ be the surrogate values without masking. Following (Covert et al., 2022), we minimize the following loss function:

$$\mathcal{L}_{exp}(\theta) = \mathop{\mathbb{E}}_{(x,y)\sim p(x,y), s\sim q(s)} \left[\left(g_\beta(x_s|y) - g_\beta(x_{\mathbf{0}}|y) - s^\top \phi_\theta(x,y) \right)^2 \right] \tag{10}$$

$$\text{s.t.} \quad \mathbf{1}^\top \phi_\theta(x,y) = g_\beta(x_{\mathbf{1}}|y) - g_\beta(x_{\mathbf{0}}|y) \quad \forall (x,y), \tag{Efficiency}$$

Notice that the explainer model $\phi_\theta(x,y)$ is being trained under a mean squared error loss, and that 16 random masks are generated for each image in the mini-batch. The explainer is hence optimized against a distribution of the Shapley values, so an accurate calculation of ground-truth Shapley values for each training sample is not even remotely necessary.

Also, the aforementioned efficiency constraint is necessary for the explainer model to output faithful and exact Shapley values. We leverage *additive efficient normalization* from (Ruiz et al., 1998) and use the same approach as prior work (Jethani et al., 2021; Covert et al., 2022) to enforce this constraint. The model is trained to make unconstrained predictions as is described in equation 10, which we then modify using the following transformation to have it constrained:

$$\phi_\theta(x,y) \leftarrow \phi_\theta(x,y) + \frac{g_\beta(x_{\mathbf{1}}|y) - g_\beta(x_{\mathbf{0}}|y) - \mathbf{1}^T \cdot \phi_\theta(x,y)}{d} \tag{11}$$

After training the explainer model, we merge the original classifier model and all relevant intermediate stages' models into one single, independent model to contain both the classification task and the explanation task to have them run concurrently. For the baseline method, ViT-shapley and its modified counterpart for NLP, no parameters overlap between the two tasks, thus inference must be done on both tasks resulting in a huge implied performance overhead. *AutoGnothi*, however, only requires a validation pass to ensure that the original classifier head is preserved verbatim in the final model. This is done by comparing the output of the original classifier and the final model on any arbitrary input.

A.6 Datasets

In this section we explain in more detail which datasets are selected and how they are processed for our experiments. Three datasets are used for the image classification task. The ImageNette dataset includes $9,469$ training samples and $3,925$ validation samples for 10 classes. MURA (musculoskeletal radiographs) has $36,808$ training samples and $3,197$ validation samples for 2 classes. The Oxford-IIIT Pets dataset contains $5,879$ training samples, 735 validation samples and 735 test samples in 37 classes. For the text classification (sequence classification) task, we use the Yelp Polarity dataset, which originally contains $560,000$ training samples and $38,000$ test samples.

For each epoch, image classifiers (ViT) iterate through all available images in either of the train or test dataset. Specifically to during training, images are normalized by the mean value and standard deviation of each corresponding training dataset, before being down-sampled to 224×224 pixels. For text classifiers, each of the epoch is trained on exactly 2048 training samples randomly chosen from the dataset, and validated on 256 equally random test samples. This is primarily done to serve our needs in frequent checkpoints for more thorough data analysis such as on CKA or parameter gradients.

Due to the sheer cost from some metrics on certain tasks, we reduced the size of our test set during evaluation. We selected 1000 test samples for datasets ImageNette, MURA and Yelp Review Polarity, and randomly selected 300 samples for the Oxford-IIIT Pets dataset. For each dataset this subset stays the same between different explanation methods and different model sizes. We emphasize that these samples are deliberately independent from the training set to avoid potential bias from the results.

B PROOFS OF THEOREMS

Here we provide detailed proof for Theorem 1 and Theorem 2, which provide theoretical guarantee for the performance of surrogates and explainers. Our proof follows (Simon & Vincent, 2020) and (Covert et al., 2022), which exhibit similar results for a single data point.

Lemma 1. *For a single input x, the expected loss under Eq. (2) is μ-strongly convex, where μ is the minimal eigenvalue of the Hessian of $\mathcal{L}_{surr}(\beta)$.*

Proof. The expected loss for a single input x under the new objective function is given by:

$$\mathcal{L}_{\text{surr}}(\beta) = \mathbb{E}_{s\sim\mathcal{U}(0,d)}\left[D_{\text{KL}}(f(x)\|g_\beta(x_s))\right]. \tag{12}$$

This loss function is convex in β because the KL divergence $D_{\text{KL}}(f(x)\|g_\beta(x_s))$ is convex in $g_\beta(x_s)$, and $g_\beta(x_s)$ is a smooth function of β. The Hessian of $\mathcal{L}_{\text{surr}}(\beta)$ with respect to β is:

$$\nabla^2_\beta\mathcal{L}_{\text{surr}}(\beta) = \mathbb{E}_{s\sim\mathcal{U}(0,d)}\left[\nabla^2_\beta D_{\text{KL}}(f(x)\|g_\beta(x_s))\right]. \tag{13}$$

The convexity of $\mathcal{L}_{\text{surr}}(\beta)$ is determined by the smallest eigenvalue of this Hessian, μ. Since the KL divergence is strictly convex, the minimum eigenvalue is positive, which implies μ-strong convexity. □

Theorem 1. *Let the surrogate model be trained using gradient descent with step size α for t iterations. The expected KL divergence between the original model's predictions $f(x)$ and the surrogate model's predictions $g_\beta(x_s)$ is upper-bounded by:*

$$\mathbb{E}_{x\sim p(x),s\sim\mathcal{U}(0,d)}\left[D_{KL}\left(f(x)\|g_\beta(x_s)\right)\right] \leq \frac{1}{2\mu}(1-\mu\alpha)^t\left(\mathcal{L}_{surr}(\beta_0) - \mathcal{L}^\star_{surr}\right), \tag{14}$$

where β_0 is the initial parameter value, and $\mathcal{L}^\star_{surr}$ is the optimal value during optimization.

Proof. Let the surrogate model be trained using gradient descent with step size α for t iterations. The optimization process for minimizing the expected KL divergence between $f(x)$ and $g_\beta(x_s)$ can be written as:

$$\beta_{t+1} = \beta_t - \alpha\nabla_\beta\mathcal{L}_{\text{surr}}(\beta_t). \tag{15}$$

Because $\mathcal{L}_{\text{surr}}(\beta)$ is μ-strongly convex, we can apply the standard result for gradient descent convergence on strongly convex functions, which gives the following bound:

$$\mathcal{L}_{\text{surr}}(\beta_t) - \mathcal{L}^\star_{\text{surr}} \leq (1-\mu\alpha)^t\left(\mathcal{L}_{\text{surr}}(\beta_0) - \mathcal{L}^\star_{\text{surr}}\right), \tag{16}$$

where $\mathcal{L}^\star_{\text{surr}}$ is the optimal value, and β_0 is the initial parameter value.

Since the KL divergence is bounded by the expected loss, we have:

$$\mathbb{E}_{x\sim p(x),s\sim\mathcal{U}(0,d)}\left[D_{\text{KL}}(f(x)\|g_\beta(x_s))\right] \leq \mathcal{L}_{\text{surr}}(\beta_t). \tag{17}$$

Substituting the bound on $\mathcal{L}_{\text{surr}}(\beta_t)$, we obtain:

$$\mathbb{E}_{x\sim p(x),s\sim\mathcal{U}(0,d)}\left[D_{\text{KL}}(f(x)\|g_\beta(x_s))\right] \leq \frac{1}{2\mu}(1-\mu\alpha)^t\left(\mathcal{L}_{\text{surr}}(\beta_0) - \mathcal{L}^\star_{\text{surr}}\right). \tag{18}$$

□

Lemma 2. *For a single input-output pair (x,y), the expected loss under Eq.(3) for the prediction $\phi_\theta(x,y)$ is μ-strongly convex with $\mu = H^{-1}_{d-1}$, where H_{d-1} is the $(d-1)$-th harmonic number.*

Proof. For an input-output pair (x,y), the expected loss for the prediction $\phi = \phi_\theta(x,y)$ is defined as

$$\begin{aligned} L_\theta(x,y) &= \mathbb{E}_{s\sim p(s)}\left[\left(g_\beta(x_s|y) - g_\beta(x_{\mathbf{0}}|y) - s^\top\phi\right)^2\right] \\ &= \phi^\top\mathbb{E}_{s\sim p(s)}[ss^\top]\phi - 2\mathbb{E}_{s\sim p(s)}\left[s\left(g_\beta(x_s|y) - g_\beta(x_{\mathbf{0}}|y)\right)\right]\phi \\ &\quad + \mathbb{E}_{s\sim p(s)}\left[\left(g_\beta(x_s|y) - g_\beta(x_{\mathbf{0}}|y)\right)^2\right]. \end{aligned} \tag{19}$$

This is a quadratic function of ϕ with its Hessian given by

$$\nabla^2_\theta L_\theta(x, y) = 2 \cdot \mathbb{E}_{s\sim p(s)}[ss^\top]. \tag{20}$$

The eigenvalues of the Hessian determine the convexity of $L_\theta(x, y)$, and the entries of the Hessian can be derived from the subset distribution $p(s)$. The distribution assigns equal probability to subsets with the same cardinality, thus we define the shorthand $p_k \equiv p(s)$ for s such that $\mathbf{1}^\top s = k$. Specifically, we have:

$$p_k = Q^{-1}\frac{d-1}{\binom{d}{k}k(d-k)} \qquad \text{and} \qquad Q = \sum_{k=1}^{d-1}\frac{d-1}{k(d-k)}. \tag{21}$$

We can then write $A \equiv \mathbb{E}_{s\sim p(s)}[ss^\top]$ and derive its entries as follows:

$$\begin{aligned}
A_{ii} &= \Pr(s_i = 1) = \sum_{k=1}^{d}\binom{d-1}{k-1}p_k \\
&= Q^{-1}\sum_{k=1}^{d-1}\frac{d-1}{d(d-k)} \\
&= \frac{\sum_{k=1}^{d-1}\frac{d-1}{d(d-k)}}{\sum_{k=1}^{d-1}\frac{d-1}{k(d-k)}}
\end{aligned} \tag{22}$$

$$\begin{aligned}
A_{ij} &= \Pr(s_i = s_j = 1) = \sum_{k=2}^{d}\binom{d-2}{k-2}p_k \\
&= Q^{-1}\sum_{k=2}^{d-1}\frac{k-1}{d(d-k)} \\
&= \frac{\sum_{k=2}^{d-1}\frac{k-1}{d(d-k)}}{\sum_{k=1}^{d-1}\frac{d-1}{k(d-k)}}.
\end{aligned} \tag{23}$$

Based on this, we observe that A has the structure $A = (b - c)I_d + c\mathbf{1}\mathbf{1}^\top$, where $b \equiv A_{ii} - A_{ij}$ and $c \equiv A_{ij}$. Following (Simon & Vincent, 2020; Covert et al., 2022), the minimum eigenvalue is given by $\lambda_{\min}(A) = b - c$. A more detailed derivation reveals that it depends on the $(d-1)$-th harmonic number, H_{d-1}:

$$\begin{aligned}
\lambda_{\min}(A) = b - c &= A_{ii} - A_{ij} \\
&= \frac{\sum_{k=1}^{d-1}\frac{d-1}{d(d-k)}}{\sum_{k=1}^{d-1}\frac{d-1}{k(d-k)}} - \frac{\sum_{k=2}^{d-1}\frac{k-1}{d(d-k)}}{\sum_{k=1}^{d-1}\frac{d-1}{k(d-k)}} \\
&= \frac{\frac{1}{d} + \sum_{k=2}^{d-1}\frac{d-k}{d(d-k)}}{\sum_{k=1}^{d-1}\frac{d-1}{k(d-k)}} \\
&= \frac{\frac{1}{d} + \frac{d-2}{d}}{\sum_{k=1}^{d-1}\frac{d-1}{k(d-k)}} \\
&= \frac{d-1}{d} \cdot \frac{1}{\sum_{k=1}^{d-1}\frac{d-1}{k(d-k)}} \\
&= \frac{1}{2\sum_{k=1}^{d-1}\frac{1}{k}} \\
&= \frac{1}{2H_{d-1}}.
\end{aligned} \tag{24}$$

The minimum eigenvalue is therefore strictly positive, implying that $L_\theta(x, y)$ is μ-strongly convex, where μ is given by

$$\mu = 2 \cdot \lambda_{\min}(A) = H_{d-1}^{-1}. \tag{25}$$

Note that the strong convexity constant μ is independent of (x, y) and is determined solely by the number of input variables d. □

Theorem 2. *Let $\phi_v(x|y)$ denote the exact Shapley value for input-output pair (x, y) in game v. The expected regression loss $\mathcal{L}_{exp}(\theta)$ upper bounds the Shapley value estimation error as follows,*

$$\mathbb{E}_{(x,y)\sim p(x,y)}\left[\left|\left|\phi_\theta(x, y) - \phi_v(x|y))\right|\right|_2\right] \leq \sqrt{2H_{d-1}\Big(\mathcal{L}_{exp}(\theta) - \mathcal{L}^\star_{exp}\Big)}, \tag{26}$$

where $\mathcal{L}^\star_{exp}$ represents the optimal loss achieved by the exact Shapley values.

Proof. We begin by considering a single input-output pair (x, y), where the prediction is given by $\phi = \phi_\theta(x, y; \theta)$. To account for the linear constraint (the Shapley value's efficiency constraint) in our objective, we write the Lagrangian $L_\theta(x, y, \gamma)$:

$$L_\theta(x, y, \gamma) = L_\theta(x, y) + \gamma\left(g_\beta(x_{\mathbf{1}}|y) - g_\beta(x_{\mathbf{0}}|y) - \mathbf{1}^\top\phi\right), \tag{27}$$

where $\gamma \in \mathbb{R}$ is the Lagrange multiplier. The Lagrangian $L_\theta(x, y, \gamma)$ is μ-strongly convex, sharing the same Hessian as $L_\theta(x, y)$:

$$\nabla^2_\theta L_\theta(x, y, \gamma) = \nabla^2_\theta L_\theta(x, y). \tag{28}$$

By strong convexity, we can bound the distance between ϕ and the global minimizer using the Lagrangian's value. Let $(\theta^\star, \gamma^\star)$ be the optimizer of the Lagrangian, such that

$$\phi_{\theta^\star}(x, y) = \phi_v(x|y), \tag{29}$$

where $\phi_v(x|y)$ is the exact Shapley value.

From the first-order condition of strong convexity, we obtain the inequality:

$$L_\theta(x, y, \gamma^\star) \geq L_{\theta^\star}(x, y, \gamma^\star) + (\phi - \phi_{\theta^\star}(x, y))^\top \nabla_\theta L_{\theta^\star}(x, y, \gamma^\star) + \frac{\mu}{2}\|\phi - \phi_{\theta^\star}(x, y)\|_2^2. \tag{30}$$

By the KKT conditions, $\nabla_\theta L_{\theta^\star}(x, y, \gamma^\star) = 0$, so the inequality simplifies to:

$$L_\theta(x, y, \gamma^\star) \geq L_{\theta^\star}(x, y, \gamma^\star) + \frac{\mu}{2}\|\phi - \phi_{\theta^\star}(x, y)\|_2^2. \tag{31}$$

Rearranging this, we get:

$$\|\phi - \phi_{\theta^\star}(x, y)\|_2^2 \leq \frac{2}{\mu}\left(L_\theta(x, y, \gamma^\star) - L_{\theta^\star}(x, y, \gamma^\star)\right). \tag{32}$$

Since ϕ is a feasible solution (i.e., it satisfies the linear constraint), this further simplifies to:

$$\|\phi - \phi_{\theta^\star}(x, y)\|_2^2 \leq \frac{2}{\mu}\left(L_\theta(x, y) - L_{\theta^\star}(x, y)\right). \tag{33}$$

Next, we take the expectation over $(x, y) \sim p(x, y)$. Denote the expected regression loss as $\mathcal{L}_{exp}(\theta)$, which is:

$$\mathcal{L}_{\text{exp}}(\theta) = \mathbb{E}_{(x,y)\sim p(x,y)}\left[\left(g_\beta(x_s|y) - g_\beta(x_{\mathbf{0}}|y) - s^\top\phi_\theta(x, y; \theta)\right)^2\right]. \tag{34}$$

Let $\mathcal{L}^\star_{\text{exp}}$ denote the loss achieved by the exact Shapley values. Taking the bound from the previous inequality in expectation, we have:

$$\mathbb{E}_{(x,y)\sim p(x,y)}\left[\|\phi_\theta(x, y; \theta) - \phi_v(x|y)\|_2^2\right] \leq \frac{2}{\mu}\left(\mathcal{L}_{\text{exp}}(\theta) - \mathcal{L}^\star_{\text{exp}}\right). \tag{35}$$

Finally, applying Jensen's inequality to the left-hand side, we obtain:

$$\mathbb{E}_{(x,y)\sim p(x,y)}\left[\|\phi_\theta(x, y; \theta) - \phi_v(x|y)\|_2\right] \leq \sqrt{\frac{2}{\mu}\left(\mathcal{L}_{\text{exp}}(\theta) - \mathcal{L}^\star_{\text{exp}}\right)}. \tag{36}$$

Substituting the value of $\mu = 1/H_{d-1}$ from Lemma 2, we conclude that:

$$\mathbb{E}_{(x,y)\sim p(x,y)}\left[\|\phi_\theta(x, y; \theta) - \phi_v(x|y)\|_2\right] \leq \sqrt{2H_{d-1}\left(\mathcal{L}_{\text{exp}}(\theta) - \mathcal{L}^\star_{\text{exp}}\right)}. \tag{37}$$

□

C DISCOVERING AND MITIGATING BIAS WITH *AutoGnothi*

In this section, we present experimental results demonstrating the ability of *AutoGnothi* to discover and mitigate bias in models. For this study, we used the ImageNette dataset and the ViT-base model. This section is divided into two parts: (1) Bias Discovery, and (2) Bias Mitigation.

C.1 BIAS DISCOVERY

First, we demonstrate that the side-branch (explainer) in our self-interpretable model can effectively capture biases present in the main branch (predictor). As shown in Figure 8(a), when an image contains potentially biased information, the predictor may make a biased prediction, often resulting in an incorrect output. The side-network identifies and explains the biased features contributing to the prediction. In a specific example, the model mistakenly treated a person and a French horn as a single object, leading to a biased prediction. The side-network successfully captured this biased feature and provided a corresponding explanation, clearly indicating the source of the bias within the prediction process.

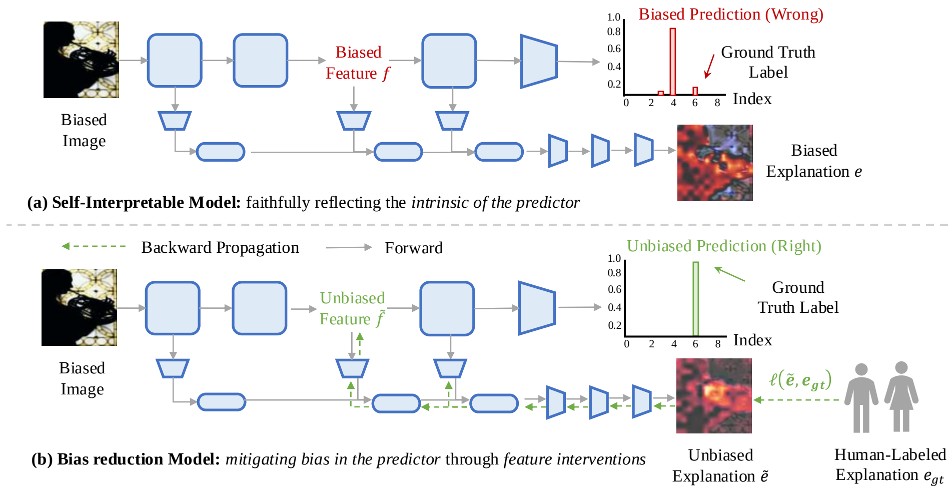

Figure 8: Bias discovery and mitigation using *AutoGnothi* on the ImageNette dataset with the side-network. (a) The original side-network is used to uncover intrinsic behaviors of the predictor, including potential biases within the model. For instance, biased associations between objects in an image can lead to incorrect predictions. The side-network identifies and explains these biases effectively. (b) A novel bias reduction pipeline is introduced to mitigate the biases discovered by the side-network. This pipeline involves performing feature intervention on biased intermediate features within the predictor. Specifically, human-labeled explanations are employed to guide the side-network's training by backpropagating the loss from the side-network to the biased feature. The biased feature is updated iteratively to reduce its influence. MSE loss is used to measure the discrepancy between the explanation map and the human-labeled explanation, ensuring alignment. After applying the pipeline, the bias in the side-network is significantly reduced, resulting in unbiased predictions by the predictor.

C.2 BIAS MITIGATION

Next, we demonstrate that the bias discovered by the side-network can be mitigated through **a novel bias reduction pipeline.** As shown in Figure 8(b), our newly designed pipeline involves performing feature intervention on biased intermediate features within the predictor. Human-labeled explanations are utilized to guide the side-network during training. Specifically, we backpropagate the loss from the side-network to the biased features, updating these features to reduce their contribution to the bias.

To achieve this, we employed Mean Squared Error (MSE) loss to quantify the difference between the explanation map produced by the side-network and the human-labeled explanation. This loss was then used to optimize the biased feature representation. Suppose that we have N patches in the explanation map of biased sample x. The loss function $\ell(e, e_{gt})$ is defined as the mean squared error (MSE) between the explanation map e produced by the side-network and the human-labeled explanation e_{gt}. The loss is calculated as follows:

$$\arg\min_{f(x)} \ell(e, e_{gt}) = \frac{1}{N}\sum_{i=1}^{N}(e_i(x) - e_{gt,i}(x))^2 \tag{38}$$

After applying the bias reduction pipeline, we observed a significant reduction in bias within the side-network, resulting in an unbiased prediction by the predictor.

For optimization, we used the SGD optimizer with a learning rate of 0.1, momentum of 0.9, and weight decay of 5×10^{-4}. The biased feature was fine-tuned over a total of 100 epochs using the biased image. This process effectively corrected the biased prediction while maintaining the integrity of the model's overall performance.

D Robustness Evaluation of *AutoGnothi*

In this section, we present a detailed analysis of the robustness of *AutoGnothi* on the ImageNette dataset. We used the ViT-base model as the base model and compared the robustness of *AutoGnothi* with ViT-Shapley (Covert et al., 2022). The robustness evaluation focuses on two aspects: (1) Out-of-Distribution (OoD) samples and (2) adversarial samples.

D.1 Out-of-Distribution (OoD) Samples

To evaluate the robustness of *AutoGnothi* on Out-of-Distribution (OoD) data, we utilized the ImageNette dataset with the ViT-base model. The ImageNette validation set served as the in-distribution data, while corrupted versions of these samples, adapted from ImageNet-C (Hendrycks & Dietterich, 2019), were used as OoD samples. Specifically, we applied the following corruption methods: `Snow`, `Frost`, `Fog`, `Impulse-noise`, `Shot-noise`, `Speckle-noise`, `Motion-blur`, and `Zoom-blur`. **Note that after applying these corruptions, the black-box ViT model still correctly classified these samples.**

Table 4: Quality metrics for *AutoGnothi* and ViT-Shapley on OoD samples.

		Snow	Frost	Fog	Impulse Noise	Shot Noise	Speckle Noise	Motion Blur	Zoom Blur
Insertion (↑)	Covert et al.	0.8755	0.9114	**0.8397**	0.9105	0.9253	0.9341	0.9064	0.8911
	AutoGnothi	**0.9015**	**0.9432**	0.8387	**0.9482**	**0.9513**	**0.9578**	**0.9212**	**0.8963**
Deletion (↓)	Covert et al.	0.5813	0.6138	0.5668	0.6129	0.6075	0.6293	0.6616	0.5543
	AutoGnothi	**0.5657**	**0.5738**	**0.4624**	**0.6065**	**0.6055**	**0.6170**	**0.6077**	**0.5319**

We first qualitatively evaluated the explanation quality of *AutoGnothi* and ViT-Shapley (Covert et al., 2022). Despite the added corruption, the black-box ViT model successfully classified these samples correctly. As shown in Figure 9 and Figure 10, *AutoGnothi* consistently captured the core object area even after corruption, whereas ViT-Shapley struggled to highlight the key information accurately. This performance gap was especially pronounced when the `fog` corruption was applied, as ViT-Shapley failed to retain essential explanation fidelity under these conditions.

Next, we conducted a quantitative evaluation of *AutoGnothi*'s robustness on OoD samples using insertion and deletion metrics. These metrics were applied to evaluate the ability of the explanations to retain key information under corruption. As shown in Table 4, *AutoGnothi* outperformed ViT-Shapley (Covert et al., 2022) in both insertion and deletion metrics across all corruption types. This result indicates that *AutoGnothi* is more robust in maintaining explanation quality under challenging OoD conditions, providing more reliable and interpretable insights into model predictions.

Our results demonstrate that *AutoGnothi* significantly outperforms ViT-Shapley (Covert et al., 2022) in both qualitative and quantitative robustness evaluations on OoD samples. These findings indicate that *AutoGnothi* is more capable of maintaining explanation quality under challenging OoD conditions, providing more reliable and interpretable insights into model predictions.

Figure 9: Robustness evaluation of *AutoGnothi* and ViT-Shapley (Covert et al., 2022) on the ImageNette dataset using the ViT-base model. We used the test samples in the ImageNette dataset as in-distribution samples and applied several corruption methods to create OoD samples. (1/2)

Figure 10: Robustness evaluation of *AutoGnothi* and ViT-Shapley (Covert et al., 2022) on the ImageNette dataset using the ViT-base model. We used the test samples in the ImageNette dataset as in-distribution samples and applied several corruption methods to create OoD samples. (2/2)

D.2 ADVERSARIAL SAMPLES

Next, we evaluated the robustness of *AutoGnothi* on adversarial samples. The test samples from the ImageNette dataset were treated as clean samples, and adversarial samples were generated using the PGD (Madry, 2017) attack. The following parameters were used for the PGD attack: number of steps = 30, perturbation magnitude $\varepsilon = 8/255$, and step size $\alpha = 2/255$. Unlike the OoD samples, the focus here is on scenarios where the black-box ViT model fails to correctly classify the adversarial samples after the attack. We evaluated whether the explaination quality of *AutoGnothi* and ViT-Shapley (Covert et al., 2022) can adapt to the shifted semantics caused by the attack, *i.e.*, shifting from the ground truth category to the misclassified (adversarial) category.

We qualitatively evaluated the explanation quality through visualizations. As shown in Figure 11, the explainers are expected to adapt to the shifted semantics caused by the attack, reflecting the new (adversarial) prediction of the black-box model. Specifically, we observed that *AutoGnothi* successfully transfers its explanation focus from the original (ground truth) class to the adversarial class predicted after the attack. In contrast, ViT-Shapley (Covert et al., 2022) fails to capture the core information for the adversarial samples, often providing inconsistent or irrelevant explanations.

This behavior underscores the importance of an explainer's ability to grasp the intrinsic mechanisms of the black-box model. Adversarial samples provide a challenging test for this capability, as they require the explainer to align with the shifted semantics of the model's prediction under adversarial perturbation. The superior performance of *AutoGnothi* in this scenario highlights its robustness and adaptability in capturing the underlying characteristics of the black-box model.

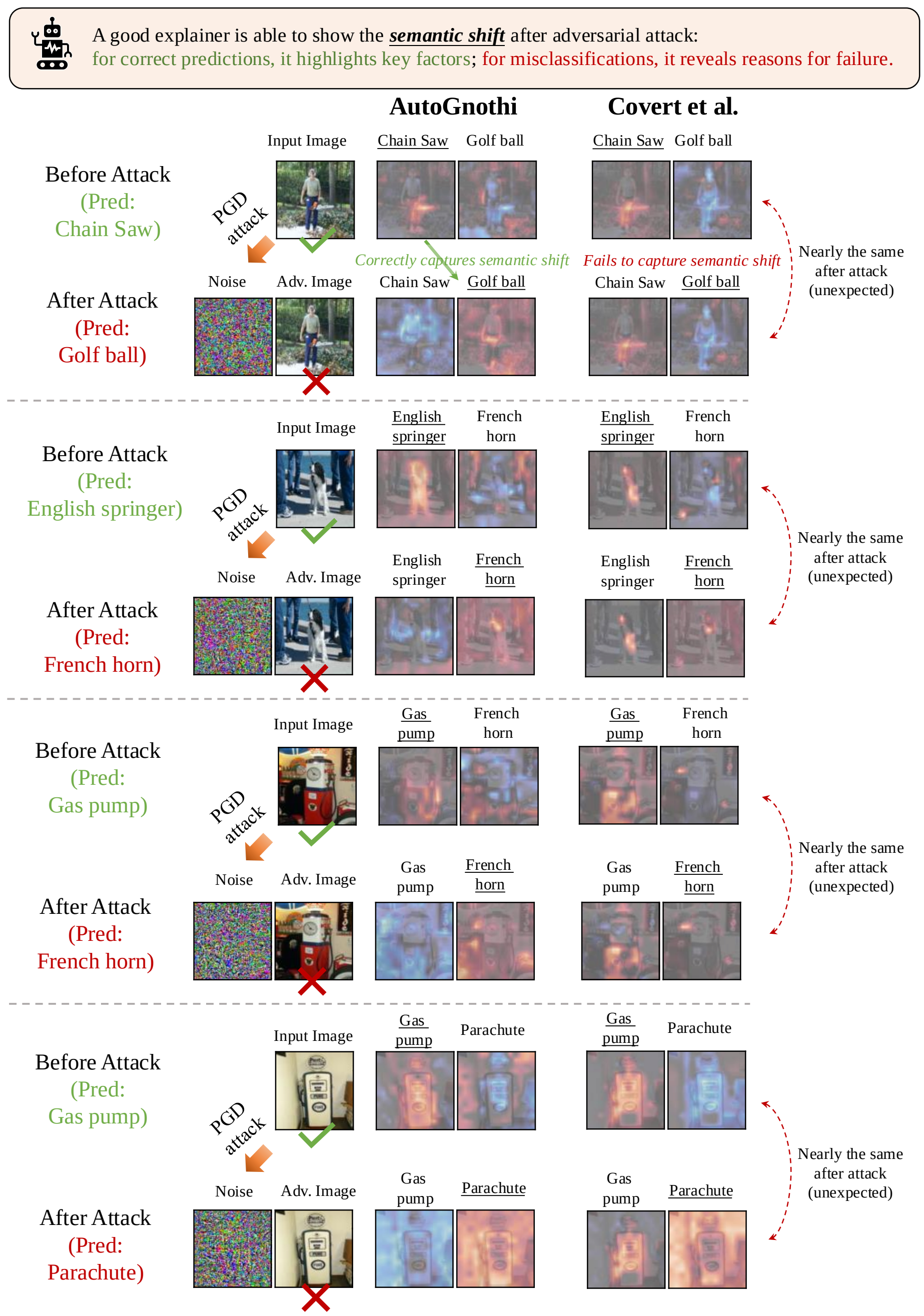

Figure 11: Robustness evaluation of *AutoGnothi* and ViT-Shapley (Covert et al., 2022) on the ImageNette dataset using the ViT-base model. Test samples were used to generate adversarial samples using the PGD attack. Explanations were computed for the original target class and the predicted class after the attack for each sample.

E ADDITIONAL RESULTS FOR *AutoGnothi*

In addition to the results on ImageNette included in the main paper, we provide more detailed results on other datasets ranging from image classification tasks to text classification tasks, against a number of baseline explanation methods, with respect to other model sizes in this section.

Table 5: Performance metrics for ViT-tiny on ImageNette.

Method	Insertion (↑)	Deletion (↓)
Random	0.9231±0.1094	0.9229±0.1106
Attention last	0.9281±0.1033	0.7311±0.2422
Attention rollout	0.9138±0.1102	0.7306±0.2449
GradCAM (Attn)	0.9155±0.1242	0.8292±0.2089
GradCAM (LN)	0.9280±0.0937	0.8436±0.2046
Vanilla (Pixel)	0.9006±0.1173	0.8161±0.2034
Vanilla (Embed)	0.9131±0.1109	0.7708±0.2272
IntGrad (Pixel)	0.9383±0.0808	0.8734±0.1817
IntGrad (Embed)	0.9317±0.0808	0.8092±0.1817
SmoothGrad (Pixel)	0.9153±0.1199	0.7724±0.2236
SmoothGrad (Embed)	0.9268±0.1092	0.7852±0.2176
VarGrad (Pixel)	0.9219±0.1147	0.7872±0.2157
VarGrad (Embed)	0.9317±0.1063	0.8092±0.2062
LRP	0.9439±0.0852	0.6883±0.2603
Leave-one-out	0.9632±0.0401	0.7671±0.2902
RISE	0.9743±0.0333	0.6514±0.3028
Covert et al.	**0.9824±0.0289**	0.5243±0.2579
AutoGnothi (Ours)	0.9802±0.0268	**0.5097±0.2688**

Table 6: Performance metrics for ViT-small on ImageNette.

Method	Insertion (↑)	Deletion (↓)
Random	0.9471±0.0827	0.9461±0.0843
Attention last	0.9599±0.0771	0.7617±0.2205
Attention rollout	0.9293±0.0940	0.8566±0.1793
GradCAM (Attn)	0.9217±0.1205	0.9301±0.1186
GradCAM (LN)	0.9239±0.0893	0.9184±0.1571
Vanilla (Pixel)	0.9535±0.1006	0.8179±0.1686
Vanilla (Embed)	0.9564±0.0894	0.8240±0.1886
IntGrad (Pixel)	0.9581±0.0738	0.9219±0.1281
IntGrad (Embed)	0.9581±0.0738	0.9219±0.1281
SmoothGrad (Pixel)	0.9542±0.0770	0.7998±0.2055
SmoothGrad (Embed)	0.9550±0.0788	0.8065±0.2090
VarGrad (Pixel)	0.9535±0.0798	0.8179±0.1954
VarGrad (Embed)	0.9564±0.0776	0.8240±0.1942
LRP	0.9636±0.0637	0.7549±0.2275
Leave-one-out	0.9684±0.0319	0.8815±0.2056
RISE	0.9773±0.0206	0.7960±0.2599
Covert et al.	**0.9828±0.0440**	0.6865±0.2255
AutoGnothi (Ours)	0.9791±0.0305	**0.6667±0.2636**

Table 7: Performance metrics for ViT-large on ImageNette.

Method	Insertion (↑)	Deletion (↓)
Random	0.9645±0.0748	0.9642±0.0757
Attention last	0.9251±0.0794	0.8997±0.1380
Attention rollout	0.9336±0.0835	0.9429±0.0997
GradCAM (Attn)	0.9398±0.0692	0.9328±0.1228
GradCAM (LN)	0.9590±0.0619	0.9366±0.1330
Vanilla (Pixel)	0.9040±0.1046	0.9372±0.1106
Vanilla (Embed)	0.9151±0.0959	0.9258±0.1237
IntGrad (Pixel)	0.9716±0.0584	0.9596±0.0948
IntGrad (Embed)	0.9716±0.0584	0.9596±0.0948
SmoothGrad (Pixel)	0.9499±0.0778	0.8953±0.1579
SmoothGrad (Embed)	0.9636±0.0681	0.8664±0.1643
VarGrad (Pixel)	0.9444±0.0827	0.9060±0.1456
VarGrad (Embed)	0.9558±0.0687	0.8827±0.1545
LRP	0.9506±0.0646	0.8814±0.1530
Leave-one-out	0.9743±0.0521	0.9534±0.1085
RISE	0.9801±0.0373	0.9245±0.1570
Covert et al.	**0.9843±0.0436**	0.7646±0.2012
AutoGnothi (Ours)	0.9837±0.0225	**0.6570±0.2171**

Table 8: Performance metrics for ViT-base on Oxford-IIIT Pet.

Method	Insertion (↑)	Deletion (↓)
Random	0.8642±0.1855	0.8625±0.1851
Attention last	0.9066±0.1302	0.5534±0.2183
Attention rollout	0.8616±0.1384	0.7387±0.2326
GradCAM (Attn)	0.8726±0.1585	0.7582±0.2296
GradCAM (LN)	0.8828±0.1137	0.7648±0.2462
Vanilla (Pixel)	0.8855±0.1362	0.6551±0.2395
Vanilla (Embed)	0.8996±0.1354	0.5783±0.2405
IntGrad (Pixel)	0.9219±0.1137	0.8451±0.1990
IntGrad (Embed)	0.9219±0.1137	0.8451±0.1990
SmoothGrad (Pixel)	0.9140±0.1329	0.5508±0.2347
SmoothGrad (Embed)	0.8731±0.1462	0.8716±0.1514
VarGrad (Pixel)	0.9145±0.1268	0.5801±0.2366
VarGrad (Embed)	0.8818±0.1437	0.8778±0.1487
LRP	0.9192±0.1178	0.5362±0.2258
Leave-one-out	0.9468±0.0666	0.7341±0.2951
RISE	**0.9581±0.0333**	0.6186±0.3096
Covert et al.	0.9422±0.1035	0.4958±0.2404
AutoGnothi (Ours)	0.9384±0.1088	**0.4888±0.2480**

Table 9: Performance metrics for ViT-base on MURA. MURA is a binary classification dataset, we calculated metrics for each of its two categories.

	Abnormal		Normal	
Method	**Insertion (↑)**	**Deletion (↓)**	**Insertion (↑)**	**Deletion (↓)**
Random	0.8195$_{\pm 0.1875}$	0.8206$_{\pm 0.1859}$	0.1548$_{\pm 0.1396}$	0.1564$_{\pm 0.1415}$
Attention last	0.8416$_{\pm 0.1863}$	0.6303$_{\pm 0.1912}$	0.1546$_{\pm 0.1365}$	0.1849$_{\pm 0.1348}$
Attention rollout	0.8047$_{\pm 0.1887}$	0.7236$_{\pm 0.2107}$	0.1758$_{\pm 0.1393}$	0.1636$_{\pm 0.1366}$
GradCAM (Attn)	0.8077$_{\pm 0.1883}$	0.8172$_{\pm 0.1925}$	0.1611$_{\pm 0.1387}$	0.1655$_{\pm 0.1518}$
GradCAM (LN)	0.8509$_{\pm 0.1787}$	0.7451$_{\pm 0.2171}$	0.1771$_{\pm 0.1537}$	0.1487$_{\pm 0.1338}$
Vanilla (Pixel)	0.8384$_{\pm 0.1764}$	0.5971$_{\pm 0.2056}$	0.1710$_{\pm 0.1401}$	0.1603$_{\pm 0.1310}$
Vanilla (Embed)	0.8412$_{\pm 0.1774}$	0.5709$_{\pm 0.1993}$	0.1666$_{\pm 0.1393}$	0.1649$_{\pm 0.1295}$
IntGrad (Pixel)	0.8677$_{\pm 0.1642}$	0.7690$_{\pm 0.2261}$	0.2011$_{\pm 0.1842}$	0.1326$_{\pm 0.1283}$
IntGrad (Embed)	0.8677$_{\pm 0.1642}$	0.7690$_{\pm 0.2261}$	0.2011$_{\pm 0.1842}$	0.1326$_{\pm 0.1283}$
SmoothGrad (Pixel)	0.8351$_{\pm 0.1893}$	0.6469$_{\pm 0.2000}$	0.1610$_{\pm 0.1428}$	0.1842$_{\pm 0.1385}$
SmoothGrad (Embed)	0.8293$_{\pm 0.1863}$	0.8006$_{\pm 0.1971}$	0.1605$_{\pm 0.1500}$	0.1552$_{\pm 0.1406}$
VarGrad (Pixel)	0.8397$_{\pm 0.1844}$	0.6667$_{\pm 0.2012}$	0.1592$_{\pm 0.1404}$	0.1813$_{\pm 0.1453}$
VarGrad (Embed)	0.8328$_{\pm 0.1841}$	0.8022$_{\pm 0.1983}$	0.1575$_{\pm 0.1461}$	0.1556$_{\pm 0.1418}$
LRP	0.8524$_{\pm 0.1786}$	0.6009$_{\pm 0.1932}$	0.1693$_{\pm 0.1459}$	0.1745$_{\pm 0.1238}$
Leave-one-out	0.8996$_{\pm 0.1336}$	0.6887$_{\pm 0.2412}$	0.2952$_{\pm 0.2235}$	0.0977$_{\pm 0.0911}$
RISE	0.9247$_{\pm 0.1037}$	0.6258$_{\pm 0.2510}$	0.3470$_{\pm 0.2431}$	0.0844$_{\pm 0.0786}$
Covert et al.	**0.9319$_{\pm 0.0795}$**	0.4199$_{\pm 0.2136}$	0.4516$_{\pm 0.2506}$	**0.0539$_{\pm 0.0478}$**
AutoGnothi (Ours)	0.9292$_{\pm 0.0597}$	**0.4116$_{\pm 0.2116}$**	**0.4563$_{\pm 0.2524}$**	0.0581$_{\pm 0.0488}$

Table 10: Performance metrics for Bert-base on Yelp Review Polarity.

Method	**Insertion (↑)**	**Deletion (↓)**
KernelShap	0.8894$_{\pm 0.1324}$	0.4624$_{\pm 0.2548}$
Covert et al.	**0.9620$_{\pm 0.0472}$**	0.1725$_{\pm 0.1176}$
AutoGnothi (Ours)	0.9588$_{\pm 0.0206}$	**0.1004$_{\pm 0.0377}$**

F ADDITIONAL RESULTS FOR *AutoGnothi* ON COMPLIATED DATASETS

We provide addtional results for *AutoGnothi* on more compliated datasets. We have shown results on ImageNette, Oxford-IIIT Pet, MURA, and Yelp Review Polarity in Section E. Here we provide results on four new datasets. Specifically, for image classification, we conducted further results on CUB-200 (Wah et al., 2011) dataset. For NLP task, we provide further results on question answering dataset BoolQ (Clark et al., 2019), and also SNLI (Bowman et al., 2015) and IMBD (Maas et al., 2011) dataset.

Additional NLP Datasets. We provide results on three NLP datasets, BoolQ, SNLI, and IMDB. BoolQ is a question answering dataset that consists of 15942 examples, each containing a question and a corresponding boolean answer. SNLI is a large-scale dataset for natural language inference, containing 570k human-annotated sentence pairs. This is a dataset for binary sentiment classification containing substantially more data than previous benchmark datasets. We provide a set of 25,000 highly polar movie reviews for training, and 25,000 for testing. There is additional unlabeled data for use as well. We pre-trained a Bert-base model on BoolQ, SNLI, and IMDB datasets. The corresponding surrogate and explainer models were obtained through our paradigm. We compared *AutoGnothi* with Covert et.al (Covert et al., 2022) on these datasets using the Bert-base model. The results are shown in Table 11. We also computed the insertion and deletion metrics for each method.

Table 11: Insertion and Deletion metrics for Bert-base on BoolQ, SNLI, and IMDB datasets.

	BoolQ		SNLI		IMDB	
Method	**Insertion ($\uparrow$)**	**Deletion ($\downarrow$)**	**Insertion ($\uparrow$)**	**Deletion ($\downarrow$)**	**Insertion ($\uparrow$)**	**Deletion ($\downarrow$)**
Covert et al.	0.9411$\pm$0.0849	0.1649$\pm$0.1407	0.8535$\pm$0.0526	0.2367$\pm$0.1172	0.9719$\pm$0.0526	0.0646$\pm$0.0665
AutoGnothi	0.9409$\pm$0.1363	0.1652$\pm$0.2007	0.8676$\pm$0.1364	0.2538$\pm$0.0892	0.9696$\pm$0.0388	0.0689$\pm$0.0487

Table 12: Training Efficiency of *AutoGnothi* on BoolQ, SNLI, and IMDB datasets.

Dataset		BoolQ	SNLI	IMDB
Classifier to be explained	Memory (MB)	815.19	815.19	815.19
	#Params (M)	109.48	109.48	109.48
	Accuracy ($\uparrow$)	0.805	0.907	0.877
Surrogate (Covert et al.)	Memory (MB)	815.19	815.19	815.19
	#Params (M)	109.48	109.48	109.48
	Accuracy ($\uparrow$)	0.712	0.633	0.779
Surrogate (*AutoGnothi*)	Memory (MB)	668.69 (-18%)	668.69 (-18%)	668.69 (-18%)
	#Params (M)	7.15 (-94%)	7.15 (-94%)	7.15 (-94%)
	Accuracy ($\uparrow$)	0.712	0.596	0.807
Explainer (Covert et al.)	Memory (MB)	6399.34	6399.34	6399.34
	#Params (M)	127.79	127.79	127.79
Explainer (*AutoGnothi*)	Memory (MB)	3441.77 (-46%)	3441.77 (-46%)	3441.77 (-46%)
	#Params (M)	17.15 (-87%)	17.15 (-87%)	17.15 (-87%)

Table 13: Inference efficiency comparison on BoolQ, SNLI, and IMDB datasets.

Dataset		BoolQ	SNLI	IMDB
Classifier + Explainer (Covert et al.)	FLOPs (G)	213.51	213.51	213.51
	Time (ms)	21.4	22.0	22.2
	#Params (M)	237.27	237.27	237.27
Self-Interpretable Model (*AutoGnothi*)	FLOPs (G)	116.66 (-45%)	116.67 (-45%)	116.66 (-45%)
	Time (ms)	15.88 (-26%)	10.2 (-54%)	10.4 (-53%)
	#Params (M)	17.15 (-93%)	17.15 (-93%)	17.15 (-93%)

We also provided visualization of the explanation generated by *AutoGnothi* on BoolQ dataset. The results are shown in Figure 12 and Figure 13.

AutoGnothi (Ours)

there were also sam' s club locations in canada, six located in ontario, in which the last location closed in2009./ are there any sam' s clubs in canada

Covert et al.

there were also sam' s club locations in canada, six located in ontario, in which the last location closed in2009./ are there any sam' s clubs in canada

AutoGnothi (Ours)

the act provides a comprehensive code of company law for the united kingdom, and made changes to almost every facet of the law in relation to companies. the key provisions are:/ does companies act 2006 apply to all companies

Covert et al.

the act provides a comprehensive code of company law for the united kingdom, and made changes to almost every facet of the law in relation to companies. the key provisions are: / does companies act2006 apply to all companies

Figure 12: Visualization of Bert-base explanation on BoolQ dataset. (1/2)

AutoGnothi (Ours)

in marketing, a corporate anniversary is a celebration of a firm' s continued existence after a particular number of years. the celebration is a media event which can help a firm achieve diverse marketing goals, such as promoting its corporate identity, boosting employee morale, building greater investor confidence, and encouraging sales. as a public relations opportunity, it is a way for a firm to tout past accomplishments while strengthening relationships with employees and customers and investors. the duration of the celebration itself can vary considerably, from an hour or day to activities happening throughout the year. many businesses use an anniversary to express gratitude for past success. generally, larger corporations have the means to stage more elaborate celebrations./ does a business have a birthday or anniversary

Covert et al.

in marketing, a corporate anniversary is a celebration of a firm' s continued existence after a particular number of years. the celebration is a media event which can help a firm achieve diverse marketing goals, such as promoting its corporate identity, boosting employee morale, building greater investor confidence, and encouraging sales. as a public relations opportunity, it is a way for a firm to tout past accomplishments while strengthening relationships with employees and customers and investors. the duration of the celebration itself can vary considerably, from an hour or day to activities happening throughout the year. many businesses use an anniversary to express gratitude for past success. generally, larger corporations have the means to stage more elaborate celebrations. / does a business have a birthday or anniversary

AutoGnothi (Ours)

the eighth season of shame less , an american comedy- drama television series based on the british series of the same name by paul abbott, was announced on december19,2016, a day after the seventh season finale. the season, which premiered on november5,2017, consisted of a total of12 episodes./ is shameless coming out with a season 8

Covert et al.

the eighth season of shameless, an american comedy- drama television series based on the british series of the same name by paul abbott, was announced on december19,2016, a day after the seventh season finale. the season, which premiered on november5,2017, consisted of a total of 12 episodes./ is shameless coming out with a season8

Figure 13: Visualization of Bert-base explanation on BoolQ dataset (2/2).

Additional Image Classification Datasets. The CUB-200 dataset is a widely-used benchmark for fine-grained visual categorization tasks, particularly in the domain of bird species classification. The dataset comprises a total of 11,788 images across 200 bird subcategories, with 5,994 images designated for training and 5,794 images for testing. We pre-trained a ViT-base model on CUB-200 train set. The corresponding surrogate and explainer model were obtained through our paradigm.

We compared *AutoGnothi* with other baseline methods on the CUB-200 test dataset using the ViT-base model. The results are shown in Figure 14. We also computed the insertion and deletion metrics for each method, and the results are summarized in Table 14. The results demonstrate that *AutoGnothi* outperforms the baseline methods in terms of both insertion and deletion metrics. The training and inference efficiency metrics are further provided in Table 15 and Table 16.

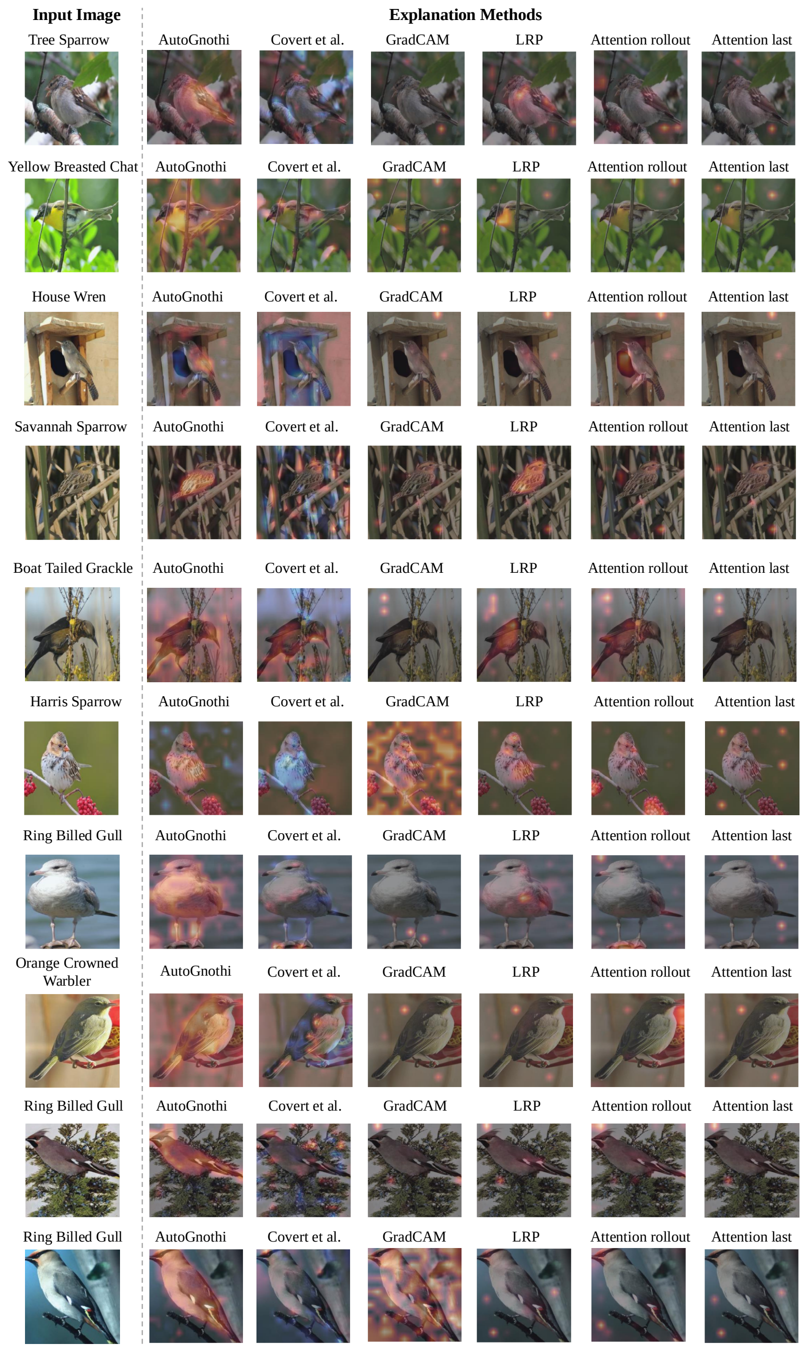

Figure 14: Visualization of ViT-base explanation on CUB-200 dataset.

Table 14: Explanation Quality Metrics for ViT-base on CUB-200 dataset.

Method	**Insertion (↑)**	**Deletion (↓)**
Random	0.4990 $\pm$0.1572	0.4599 $\pm$0.1460
Attention last	0.5888 $\pm$0.1722	0.2229 $\pm$0.1213
Attention rollout	0.5862 $\pm$0.1774	0.1606 $\pm$0.0663
LRP	0.6191 $\pm$0.1777	0.1018 $\pm$0.0430
GradCAM	0.4855 $\pm$0.1772	0.4051 $\pm$0.2063
Covert et al.	0.5096 $\pm$0.1841	0.3045 $\pm$0.2355
AutoGnothi (Ours)	**0.6234** $\pm$**0.1665**	**0.0903** $\pm$**0.0449**

Table 15: Training Efficiency of *AutoGnothi* on CUB-200 dataset.

Classifier to be explained	Memory (MB)	1313.61
	#Params (M)	85.95
	Accuracy (↑)	0.8436
Surrogate (Covert et al.)	Memory (MB)	1313.61
	#Params (M)	85.95
Surrogate (*AutoGnothi*)	Memory (MB)	710.39 (-46%)
	#Params (M)	24.91 (-71%)
Explainer (Covert et al.)	Memory (MB)	1609.49
	#Params (M)	105.30
Explainer (*AutoGnothi*)	Memory (MB)	758.93 (-53%)
	#Params (M)	28.10 (-73%)

Table 16: Inference efficiency comparison on CUB-200 datasets.

Dataset		CUB-200
Classifier + Explainer (Covert et al.)	FLOPs (G)	75.13
	Time (ms)	72.75
	#Params (M)	191.26
Self-Interpretable Model (*AutoGnothi*)	FLOPs (G)	44.78 (-40%)
	Time (ms)	61.59 (-15%)
	#Params (M)	114.05 (-40%)

G Ablation Study on the Size of Side-Networks

In this section, we present an ablation study on the architecture and size of side-networks in *AutoGnothi*. Specifically, we investigated the effect of varying the reduction factor ($r = 2, 4, 8, 16, 32$) on the side-networks of ViT-base model. To evaluate the impact, we compared the performance of *AutoGnothi* with Covert et al. (Covert et al., 2022) on the ImageNette dataset. The evaluation was performed using the insertion and deletion metrics, and the results are summarized in Table 17.

This study aimed to assess the balance between computational efficiency and explanation quality under different configurations of the side-network. The findings are as follows:

- **Too Large r:** When the reduction factor r was too large (resulting in a very small side-network), the network lacked sufficient capacity to learn the explanations effectively. As a result, the explanation quality degraded, with the side-network failing to capture enough information from the main branch.
- **Too Small r:** Conversely, when r was too small (resulting in a larger side-network), the network consumed excessive computational resources and interfered with the shared features of the predictor. This interference reduced the feature similarity between the prediction and explanation tasks, negatively impacting the faithfulness of the explainer.
- **Moderate r:** A moderate reduction factor (*e.g.*, $r = 8$) provided the optimal trade-off between computational efficiency and explanation quality. This configuration allowed the side-network to effectively utilize the features from the predictor while maintaining resource efficiency.

These results highlight the importance of carefully selecting the reduction factor to optimize the performance of *AutoGnothi* across different transformer architectures. The identified trade-offs ensure that the side-network remains both effective and efficient, making it suitable for various applications.

Table 17: Explanation Quality Metrics of the ViT-base Explainer on ImageNette dataset.

Method	**Insertion** (↑)	**Deletion** (↓)
Covert et al.	$0.9839_{\pm 0.0375}$	$0.8121_{\pm 0.1768}$
AutoGnothi (r=2)	$0.9894_{\pm 0.0329}$	$0.8687_{\pm 0.1806}$
AutoGnothi (r=4)	$0.9857_{\pm 0.0251}$	$0.7846_{\pm 0.1957}$
AutoGnothi (r=8)	$0.9874_{\pm 0.0265}$	$0.7954_{\pm 0.2294}$
AutoGnothi (r=16)	$0.9720_{\pm 0.0288}$	$0.6202_{\pm 0.2023}$
AutoGnothi (r=32)	$0.9520_{\pm 0.0443}$	$0.5547_{\pm 0.1941}$

H INTERGRATING PATCHDROPOUT TO *AutoGnothi*

The core of the *AutoGnothi* it to obtain the explainer for the self-interpretable model through side-tuning. This procedure involes obtaining a surrogate model to guide the explainer. The only reason we have to train the surrogate model, just like (Covert et al., 2022), is that the black-box models cannot fit the masked distribution. Indeed, if we can train the black-box model with the masked distribution, we can directly use the explainer to explain the black-box model. In this section, we show that we can train the black-box model with the masked distribution using PatchDrop (Liu et al., 2022).

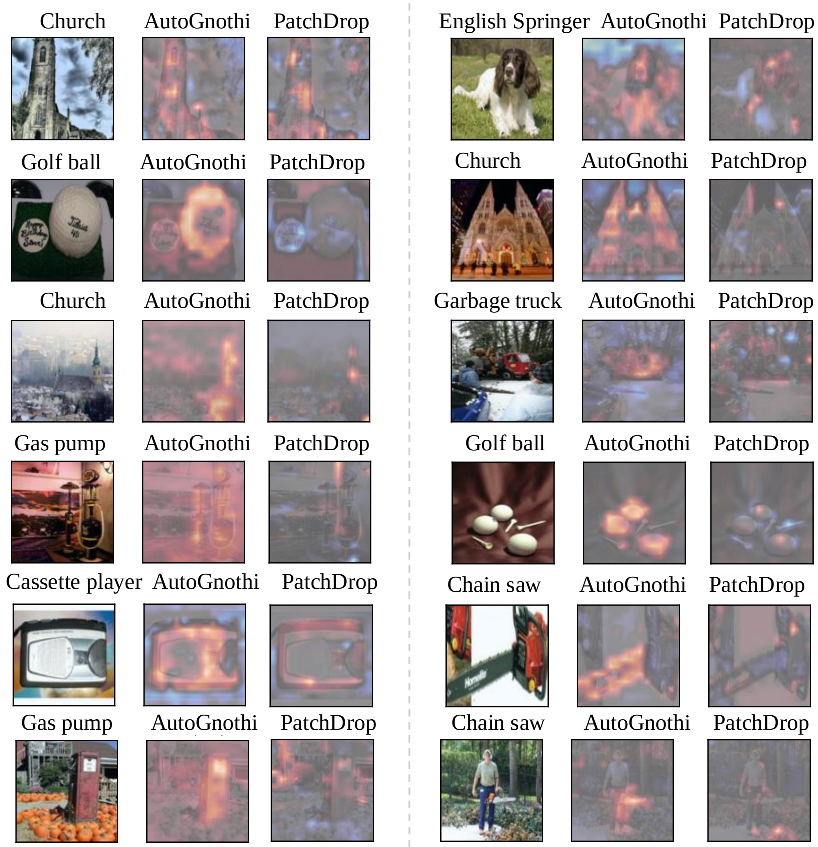

Figure 15: Comparison of the explanation quality of *AutoGnothi* with and without PatchDropout on ImageNette dataset.

As shown in Figure 15, we compared the performance of *AutoGnothi* with and without PatchDropout on the ImageNette dataset. The results demonstrate that PatchDropout did not obtain the comparative explanation quality of *AutoGnothi*.

Table 18 shows the comparison of the explanation quality of *AutoGnothi* with and without PatchDropout on the ImageNette dataset. The results demonstrate that PatchDropout did not obtain the comparative explanation quality of *AutoGnothi*.

Table 18: Quality metrics (insertion and deletion) for target class explanations of ViT-base across baseline methods and *AutoGnothi* on the ImageNette dataset.

Explanation Method	Insertion ↑ (target)	Deletion ↓ (target)
Random	0.3618±0.2136	0.4993±0.2138
Attention last	0.4393±0.2148	0.4095±0.2071
Attention rollout	0.4177±0.2006	0.3780±0.2108
GradCAM	0.4713±0.2112	0.4818±0.2207
LRP	0.6274±0.1986	0.2077±0.1751
Covert et al. w/ PatchDropout	0.7946±0.2269	0.18655±0.0535
AutoGnothi w/ PatchDropout	0.8016±0.1223	0.1299±0.1377

I Human-in-the-loop Evaluation for *AutoGnothi*

The objective of this study is to evaluate the utility of explanation methods (ViT-Shapley and *AutoGnothi*) by assessing their impact on participants' ability to predict a model's output $f(x)$. Following (Colin et al., 2022), we designed a human-in-the-loop evaluation to determine whether explanation heatmaps improve prediction accuracy and whether *AutoGnothi* offers superior utility compared to ViT-Shapley.

Datasets: We curated 15 images for each dataset, including ImageNette, Oxford-IIIT Pets, and MURA datasets, split into:

- **Training Phase:** 5 samples for participant training (for each session).
- **Testing Phase:** 10 samples for evaluation.

Each sample included: (1) an image (x), (2) its true label (y), (3) the model's prediction ($f(x)$), and (4) heatmaps from ViT-Shapley ($\phi_A(f, x)$) and *AutoGnothi* ($\phi_B(f, x)$).

For the ImageNette and Oxford-IIIT Pets datasets, testing is conducted over two sessions. Each session includes samples from only one category. For the MURA dataset, testing is conducted in a single session, as it involves a binary classification task. Specifically, the model is trained to predict whether a medical image is abnormal or not. Therefore, when the true label is provided, all possible labels are inherently covered.

Procedure:

- **Training Phase:** Participants (ψ) were trained to predict the model's output using images and heatmaps, receiving feedback on their predictions.
- **Testing Phase:** Participants evaluated 10 samples under three conditions:
  1. **Case 1:** Image (x), label (y), and prediction ($f(x)$) without heatmaps.
  2. **Case 2:** Image (x), label (y), prediction ($f(x)$), and ViT-Shapley heatmaps ($\phi_A(f, x)$).
  3. **Case 3:** Image (x), label (y), prediction ($f(x)$), and *AutoGnothi* heatmaps ($\phi_B(f, x)$).

  Participants predicted $f(x)$ for each sample and rated heatmap clarity and utility (Cases 2 and 3). Test samples were presented in randomized order without feedback to ensure unbiased evaluation.

The questionnaire is included in the supplementary materials for reference.

We measure explanation utility using the Utility-K metric:

$$\text{Utility-K} = \frac{\mathbb{P}(\psi^{(K)}(x) = f(x))}{\mathbb{P}(\psi^{(0)}(x) = f(x))}$$

where $\psi^{(K)}$ and $\psi^{(0)}$ are human meta-predictors trained with and without heatmaps, respectively. Higher Utility-K indicates more effective explanations. Aggregating over varying K, we compute the Area Under the Curve (AUC) of Utility-K values to derive the Utility score:

$$\text{Utility} = \text{AUC}(\mathcal{C}),$$

where $\mathcal{C} = \{(K_0, \text{Utility-K}_{K_0}), \ldots, (K_n, \text{Utility-K}_{K_n})\}$. Higher Utility scores represent better explanation utility.

The intuitive procedure of the whole human-in-the-loop pipeline is shown in Figure 16. The participants were trained to predict the model's output using images and heatmaps, receiving feedback on their predictions. In the testing phase, participants evaluated 10 samples under three conditions: (1) image, label, and prediction without heatmaps, (2) image, label, prediction, and ViT-Shapley heatmaps, and (3) image, label, prediction, and *AutoGnothi* heatmaps. Participants predicted the model's output for each sample and rated heatmap clarity and utility. Test samples were presented in randomized order without feedback to ensure unbiased evaluation. Due to time and resource constraints, the study was conducted with 5 participants, comprising volunteers with basic familiarity with machine learning concepts, such as students or researchers, but none of them is related to this work. While the sample size is small, the evaluation setup was carefully controlled to ensure fair comparison between explanation methods. Participants were trained uniformly, and test cases were randomized to reduce bias.

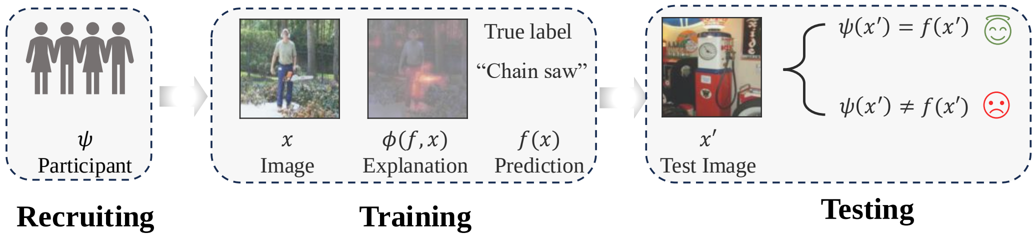

Figure 16: Human-in-the-loop evaluation procedure.

Table 19: Utility-K and Utility scores for ViT-Shapley and *AutoGnothi*. Bolded values are statistically significant improvements.

Method	**ImageNette**			**Oxford-IIIT Pets**			**MURA**	
	Session 1	**Session 2**	**Utility**	**Session 1**	**Session 2**	**Utility**	**Session 1**	**Utility**
ViT-Shapley (ϕ_A)	62.0	58.0	1.00	72.0	70.0	1.10	61.0	1.0
AutoGnothi (ϕ_B)	74.0	72.0	1.20	70.0	73.0	1.10	70.0	1.2

The Utility-K and Utility metrics are normalized and aggregated using the AUC metric. This study is intended to provide initial insights into the relative performance of *AutoGnothi* and ViT-Shapley in aiding human predictions.

Table 19 presents Utility-K and Utility scores for ViT-Shapley (ϕ_A) and *AutoGnothi* (ϕ_B) across three datasets. These results confirm that *AutoGnothi* provides more effective and interpretable explanations, significantly aiding human predictions compared to ViT-Shapley.

J ADDITIONAL VISUALIZATIONS FOR *AutoGnothi*

In this section we present a number of image samples on the ViT-base model, regarding explanation outputs from 12 representative baseline explanation methods. We ensure that these samples correspond to correct model predictions made by the base model to ensure better clarity.

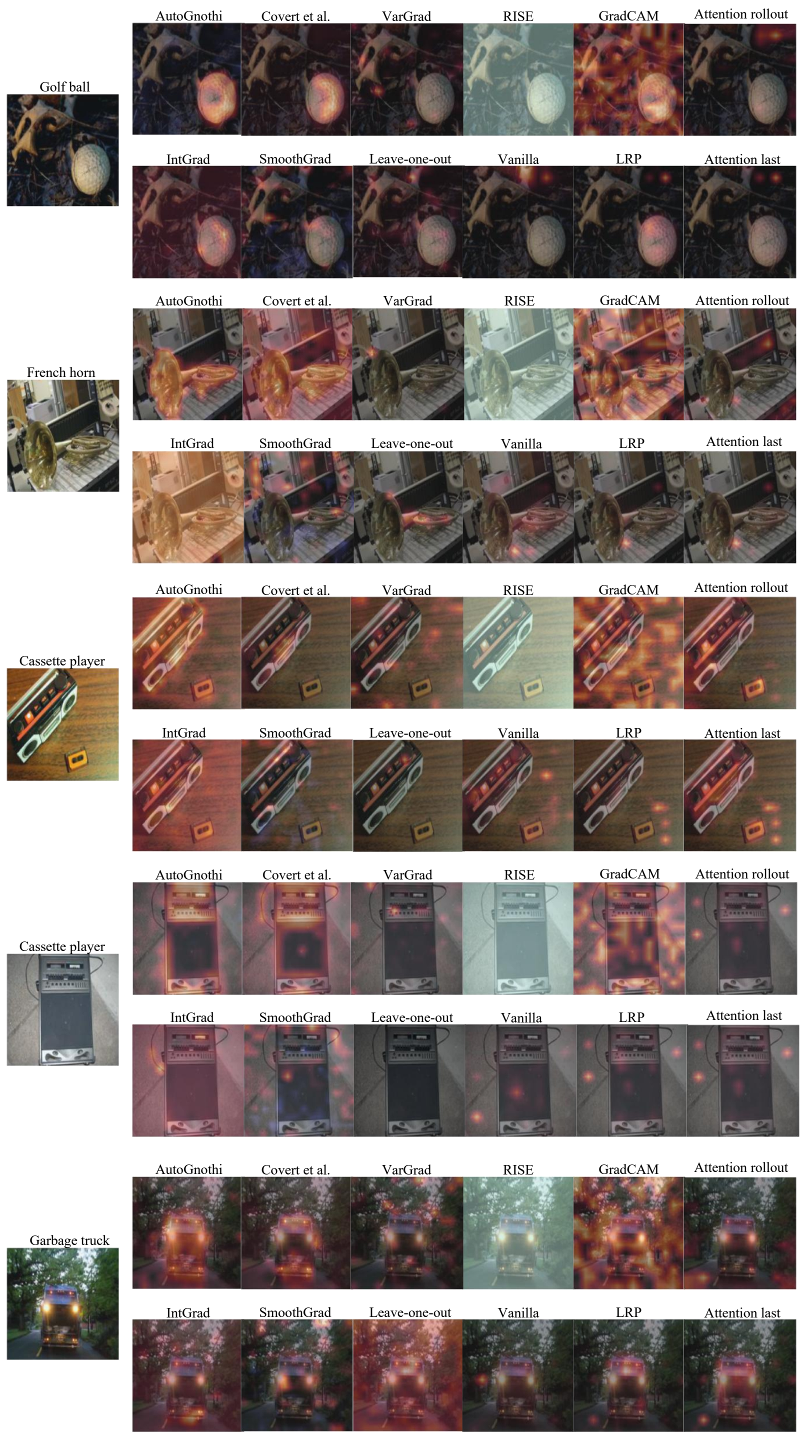

Figure 17: Visualization of ViT-base explanation on ImageNette dataset (1/2).

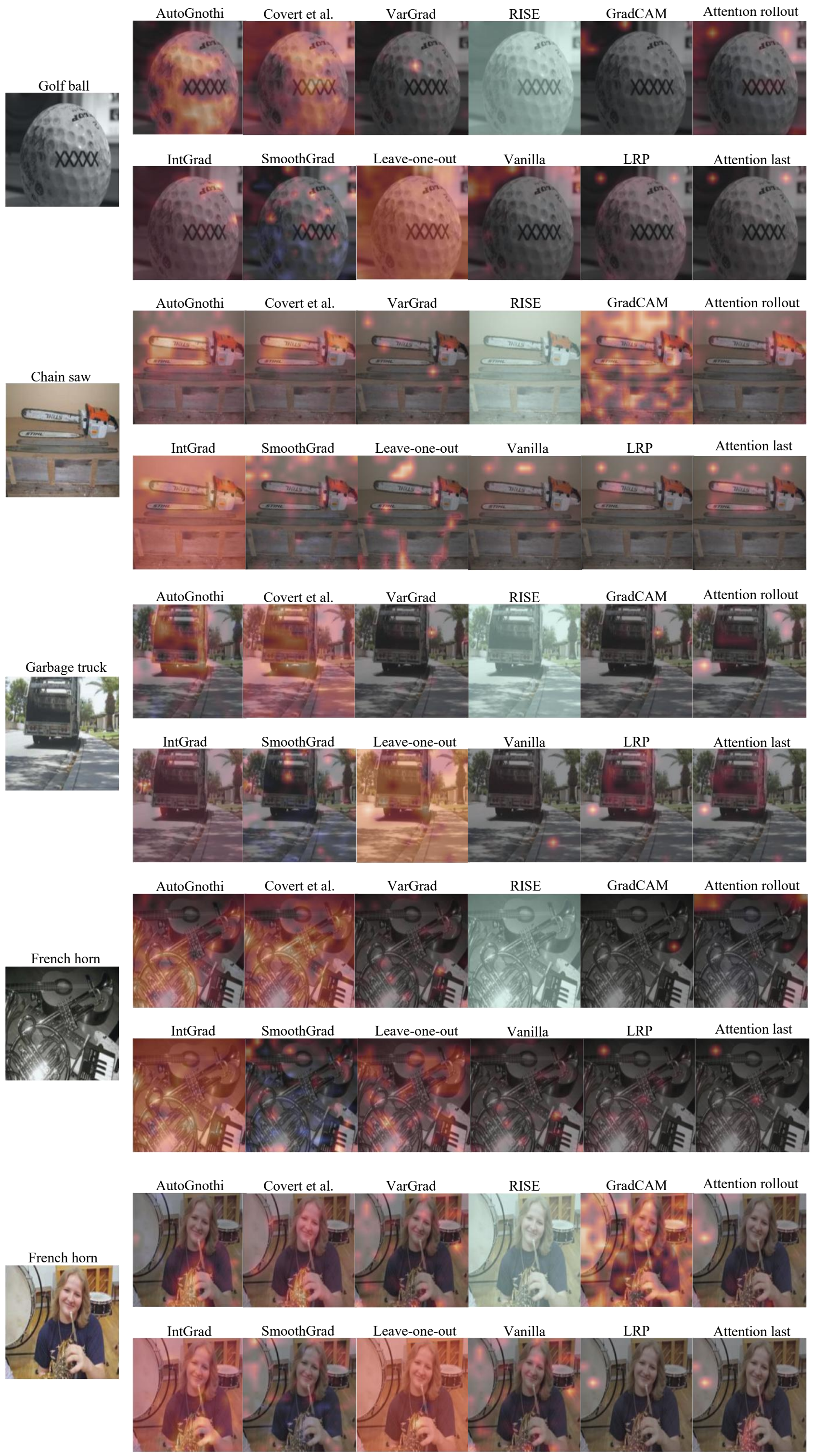

Figure 18: Visualization of ViT-base explanation on ImageNette dataset (2/2).

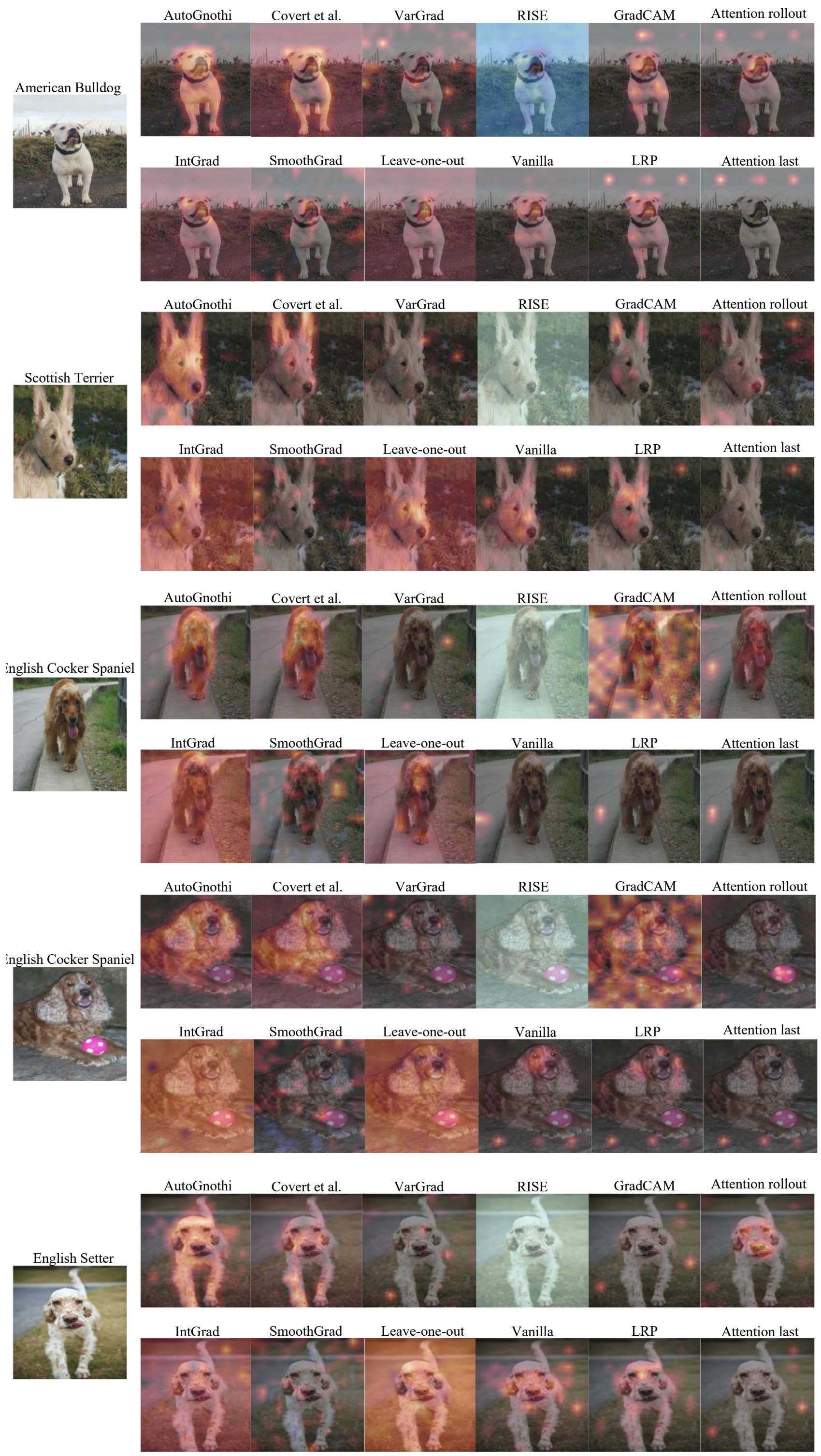

Figure 19: Visualization of ViT-base explanation on Oxford-IIIT Pet dataset (1/2).

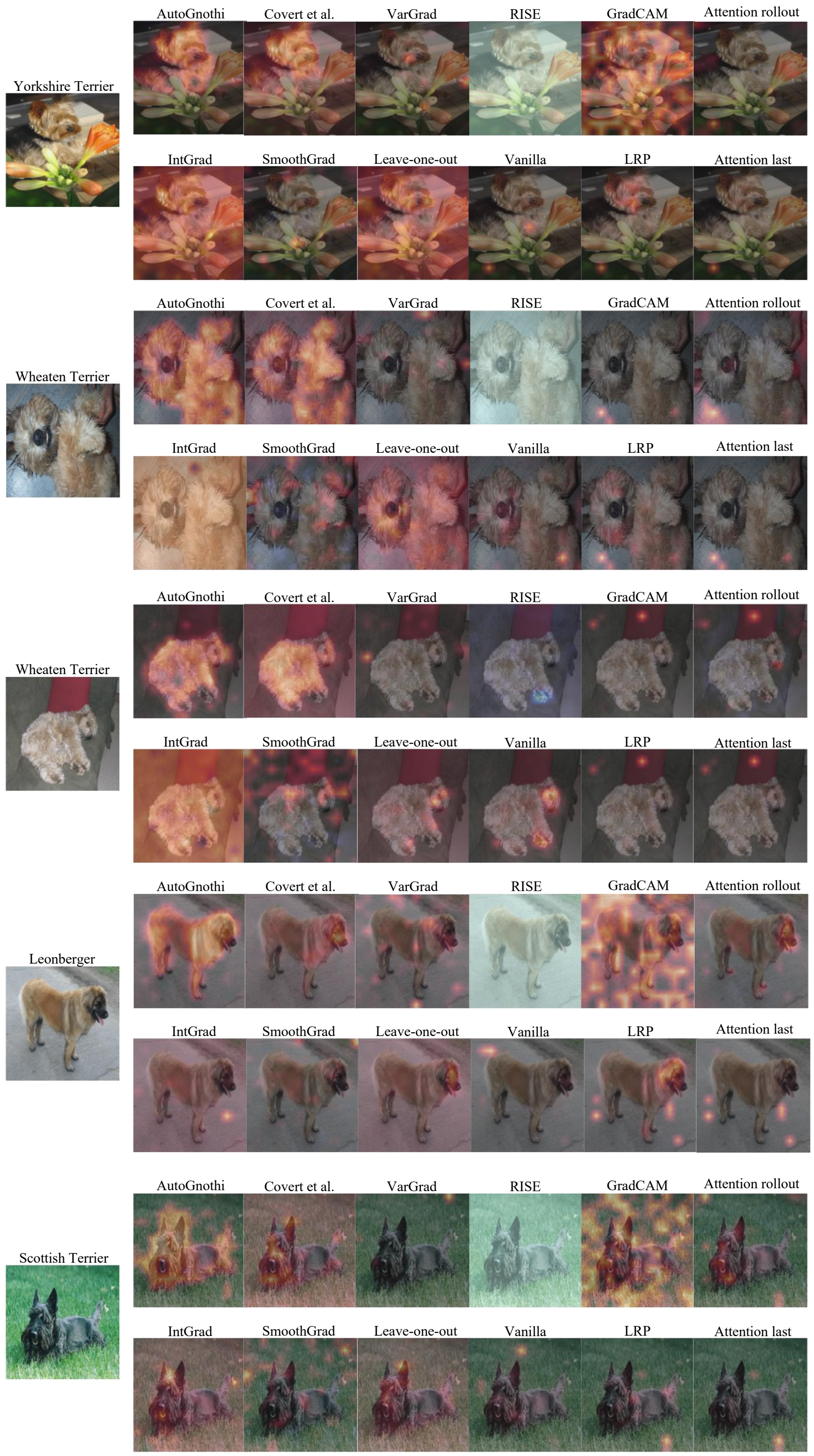

Figure 20: Visualization of ViT-base explanation on Oxford-IIIT Pet dataset (2/2).

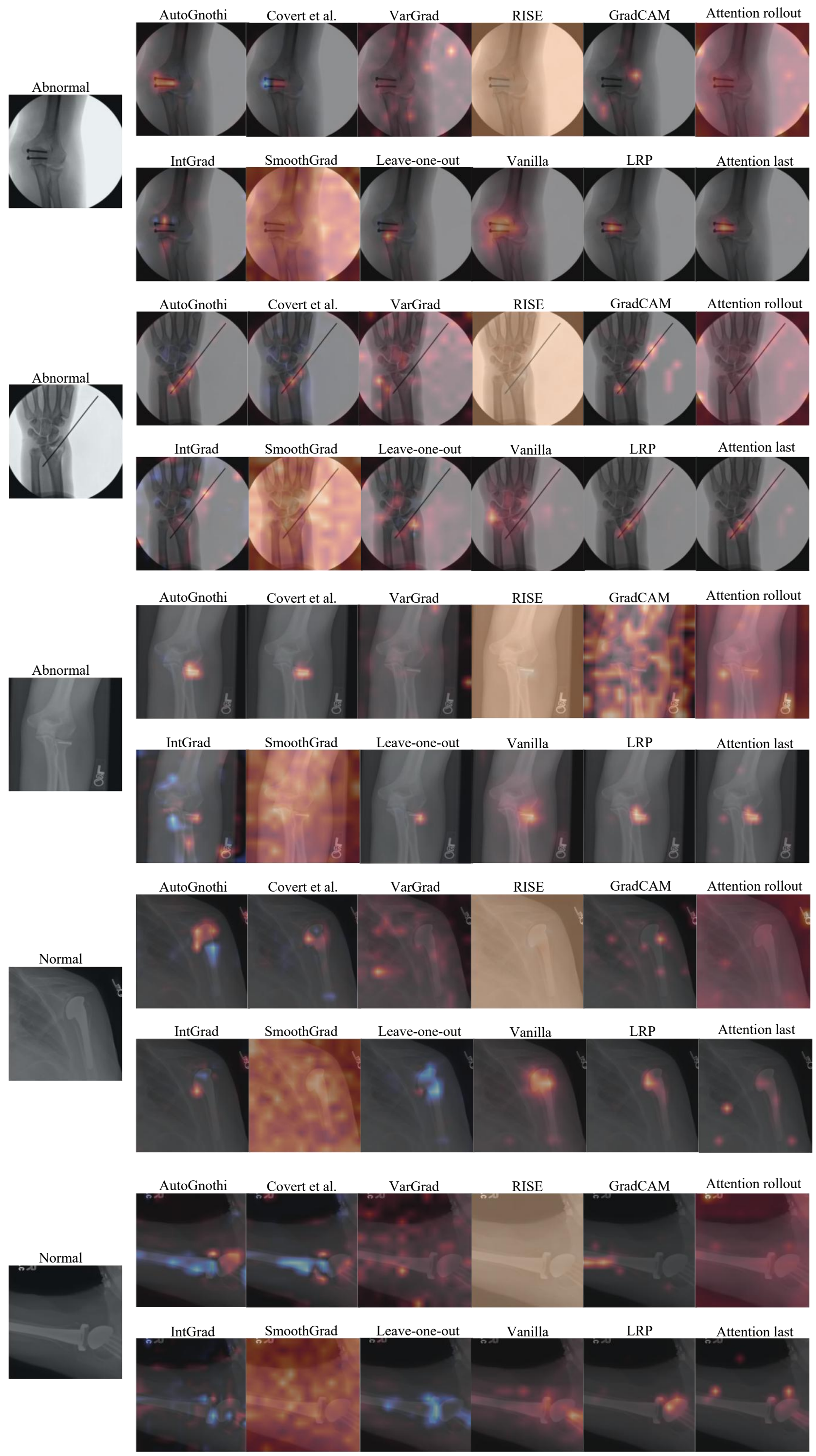

Figure 21: Visualization of ViT-base explanation on MURA dataset (1/2).

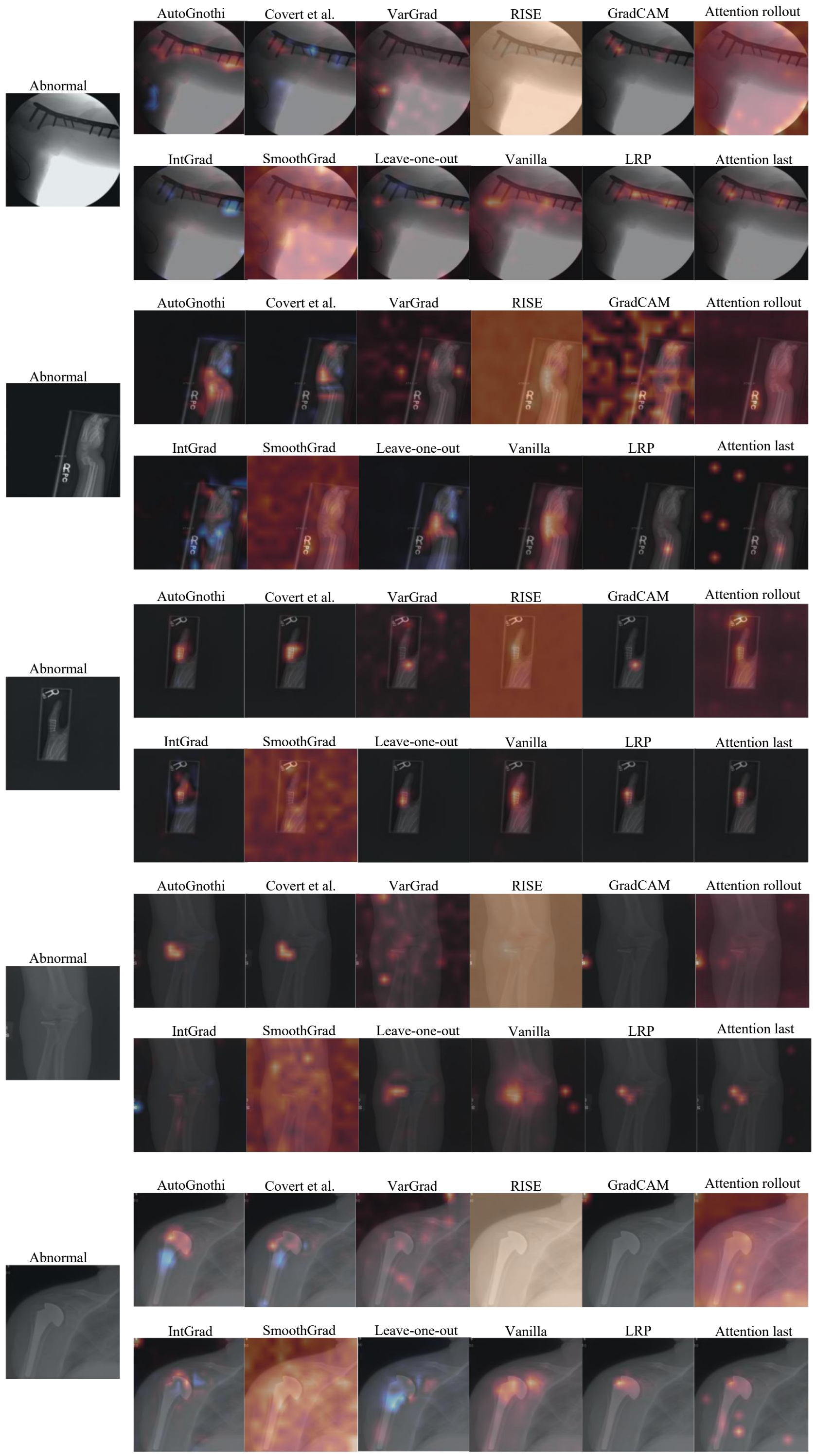

Figure 22: Visualization of ViT-base explanation on MURA dataset (2/2).